



Nanostructured Mn-based oxides for Electrochemical Energy Storage and Conversion

Journal:	<i>Chemical Society Reviews</i>
Manuscript ID:	CS-REV-06-2014-000218.R1
Article Type:	Review Article
Date Submitted by the Author:	23-Aug-2014
Complete List of Authors:	Chen, Jun; Nankai Univ, Inst New Energy Mater Zhang, Kai; Nankai Univ, Han, Xiaopeng; Institute of New Energy Material Chemistry, Chemistry College Hu, Zhe; Nankai Univ, Key Lab Adv Energy Mat Chem Zhang, Xiaolong; Nankai Univ, Tao, Zhanliang; Nankai Univ, Key Lab Adv Energy Mat Chem; Nankai Univ,

ARTICLE

Nanostructured Mn-based oxides for Electrochemical Energy Storage and Conversion

Cite this: DOI: 10.1039/x0xx00000x

Kai Zhang, Xiaopeng Han, Zhe Hu, Xiaolong Zhang, Zhanliang Tao and Jun Chen*

Received 00th January 2012,
Accepted 00th January 2012

DOI: 10.1039/x0xx00000x

www.rsc.org/

Batteries and supercapacitors as electrochemical energy storage and conversion devices are continuously serving for human life. The electrochemical performance of batteries and supercapacitors depends in large part on the active materials in electrodes. As an important family, Mn-based oxides have shown versatile applications in primary batteries, secondary batteries, metal–air batteries, and pseudocapacitors due to their high activity, high abundance, low price, and environmental friendliness. In order to meet future market demand, it is essential and urgent to make further improvements on energy and power densities of Mn-based electrode materials with the consideration of multiple electron reaction and low molecular weight of the active materials. Meanwhile, nanomaterials are favourable to achieve high performance by means of shortening the ionic diffusion length and providing large surface areas for electrode reactions. This article reviews the recent efforts to apply nanostructured Mn-based oxides for batteries and pseudocapacitors. The influence of structure, morphology, and composition on electrochemical performance has been systematically summarized. Compared to bulk materials and notable metal catalysts, nanostructured Mn-based oxides can promote the thermodynamics and kinetics of the electrochemical reactions occurring at the solid–liquid or solid–liquid–gas interface. In particular, nanostructured Mn-based oxides such as one-dimension MnO_2 nanostructures, MnO_2 /conductive matrix nanocomposites, concentration-gradient structured layered Li-rich Mn-based oxides, porous $\text{LiNi}_{0.5}\text{Mn}_{1.5}\text{O}_4$ nanorods, core-shell structured $\text{LiMnSiO}_4@\text{C}$ nanocomposites, spinel-type Co–Mn–O nanoparticles, and perovskite-type CaMnO_3 with micro-nano structures all display superior electrochemical performance. This review should shed light on the sustainable development of advanced batteries and pseudocapacitors with nanostructured Mn-based oxides.

1. Introduction

Electrochemical energy storage and conversion devices such as batteries and supercapacitors have been widely applied in the fields of portable electronic products, electric vehicles, and smart electrical grids. Systems of electrochemical energy storage and conversion such as Li-ion batteries (LIBs), Li– O_2 batteries, fuel cells, and supercapacitors have been particularly developed.^{1–3} The electrode materials which directly participate in or indirectly catalyze electrochemical reactions play a key role in improving the capability of energy storage and promoting the efficiency and rate of energy conversion.^{4–6} Among various electrode materials, Mn-based oxides have received a lot of interests because of high nature abundance, low price as well as various crystal structures and phases (Fig. 1).^{7–10} Furthermore, Mn-based oxides have versatile applications and excellent performance in the field of electrochemical energy storage and conversion. For examples, nanostructured MnO_2 exhibits outstanding discharge capacity in primary Zn– MnO_2 batteries and specific capacitance in pseudocapacitance,^{11, 12} spinel-type $\text{LiNi}_{0.5}\text{Mn}_{1.5}\text{O}_4$ displays a

high discharge plateau and superior cycling and rate performance in LIBs,^{13, 14} and perovskite CaMnO_3 delivers high oxygen reduction potential and large current density in oxygen reduction reactions.¹⁵ The recent efforts to employ nanostructured Mn-based oxides for batteries and capacitors with high energy and power density have been widely investigated. However, fully consideration for the relationship between nanostructure and electrochemical performance is still limited. It is thus that this article reviews the advantages and challenges of nanostructured Mn-based oxides for the applications of electrochemical energy storage and conversion such as in the fields of batteries and supercapacitors.

As the nanoscience and nanotechnology develop, nanostructured materials have attracted more and more people's attention, especially in the field of electrochemical energy storage and conversion. Previous studies have demonstrated that the size effects of nanostructured materials to some extent improve the thermodynamics and kinetics of electrochemical reactions. In batteries, electrochemical reactions of the electrodes are the bridge of conversion between electrical and chemical energy. According to the thermodynamic principle,

electrochemical transformation obeys the basic thermodynamic equations as follows:^{16,17}

$$ED = E \times Q \quad (1)$$

$$E = -\frac{\Delta G}{nF} \quad (2)$$

$$Q = \frac{nF}{3.6M_w} \quad (3)$$

where ED is the energy density, E is the electromotive force of an electrochemical reaction, Q is the theoretical gravimetric specific capacity, ΔG is the Gibbs free energy change, n is the electron transferred number in stoichiometric reaction, F is the Faraday constant, and M_w is the equivalent molecular weight. Because energy density is the product of Q and E, high energy density means high voltage and high capacity. High voltage originates from high chemical potential of cathode materials and low chemical potential of anode materials, while high capacity derives from multiple electron reaction and low molecular weight of the active materials (Fig. 2a). Nanostructures can improve energy density.¹⁸ On one hand, nanostructure can increase the utilization of the active materials and initiate new lithium storage space such as micropores, leading to higher capacity than bulk counterparts. On the other hand, nanostructure can reduce the polarization of the electrochemical reaction to enhance the working voltage. In addition, some electrochemical reactions cannot occur in bulk counterparts, unless turning the active materials into nanosize or nanoporous structures.^{18, 19} Among various electrode materials, Mn-based oxide nanomaterials show outstanding properties. For example, Li-rich layered $\text{Li}(\text{Li}_{1/3-2x/3}\text{M}_x\text{Mn}_{2/3-x/3})\text{O}_2$ with low molecular weight delivers a high specific capacity of $\sim 300 \text{ mAh g}^{-1}$. Spinel-type $\text{LiNi}_{0.5}\text{Mn}_{1.5}\text{O}_4$ has a high operating voltage of around 4.7 V vs. Li^+/Li .¹⁴ Polyanion-type $\text{Li}_2\text{MnSiO}_4$ can achieve a two-electron exchange reaction with a theoretical capacity of 333 mAh g^{-1} in LIBs.²⁰

In comparison, metal–air batteries have shown larger theoretical specific energy than that of lithium-ion batteries. For instance, Li–air system possesses a theoretical specific energy of nearly 11700 Wh kg^{-1} (for anode). However, the oxygen cathode of metal–air cell needs efficient catalyst to promote the sluggish kinetics. Nanostructured materials with porous features and relatively larger surface areas favor the electrolyte immersion and Li^+ ion/oxygen diffusion, inducing more active contact sites than bulk counterparts. Nevertheless, traditional catalysts are mainly notable metal nanocrystals which are rare and expensive, so it is difficult to achieve future widespread development of metal–air batteries. Owing to low cost and high abundance of Mn-based oxides, developing nanostructured Mn-based oxides have attracted extensive attention. Mn-based oxides (e.g., MnO_2 , spinel $\text{Co}_x\text{Mn}_{3-x}\text{O}_4$, and perovskite CaMnO_3) along with various nanostructures all deliver high catalytic activity of oxygen reduction/evolution reactions in metal–air batteries.²¹⁻²³ Therefore, Mn-based oxides as nonprecious electrocatalysts exhibit sustainable application prospects.

In supercapacitors, energy density can be calculated as follows:²⁴

$$ED = \frac{1}{2}CE^2 \quad (4)$$

$$C = \frac{A\varepsilon}{4\pi d} \quad (5)$$

where C is the capacitance, A is the area of the electrode surface, ε is the medium dielectric constant, and d is the effective thickness of the electrical double layer. For electrical double layer capacitors (EDLCs), only $0.17\text{--}0.20 \text{ e}^-$ per atom is adsorbed on the surface of electrode materials.²⁵ Recently, pseudocapacitors are particularly attractive because of their battery-level energy density.²⁶ Nanostructure has large surface area to achieve high capacitance, and MnO_2 as the electrode materials of pseudocapacitors possesses a theoretical specific capacitance of 1370 F g^{-1} .⁷ However, the practical capacitance is only $200\text{--}600 \text{ F g}^{-1}$, so the full potential of Mn-based oxides needs to be further exploited.

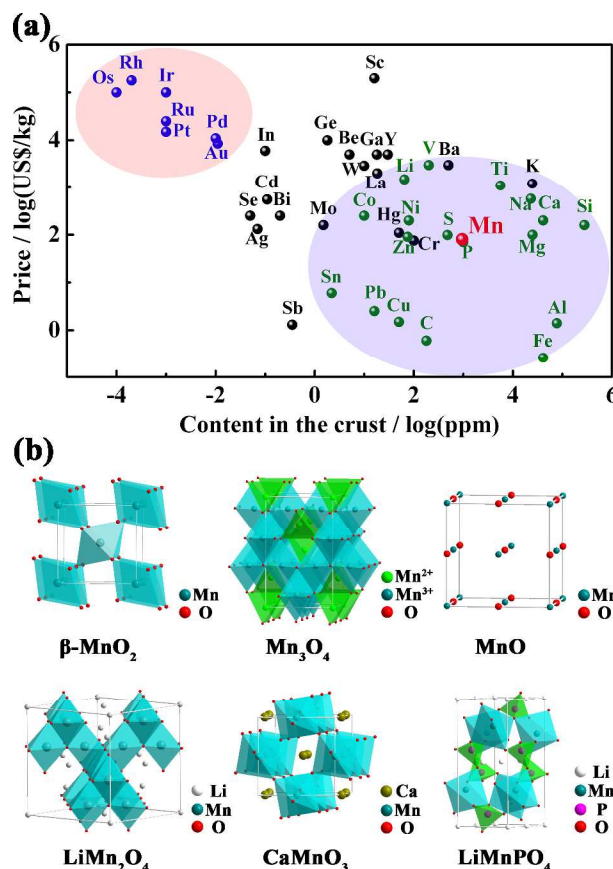


Fig. 1. (a) The plots of price obtained from Handbook of Chemistry and Physics to content in the earth's crust of elements (noble elements: blue, common elements: olive, Mn element: red, other elements: black; noble element zone: light pink, satisfactory element zone: light purple). (b) Crystal structure of rutile $\beta\text{-MnO}_2$, tetragonal spinel Mn_3O_4 , rock salt MnO , cubic spinel LiMn_2O_4 , perovskite CaMnO_3 , and olivine LiMnPO_4 .

Thermodynamics describe the maximum energy release or storage for an electrochemical reaction, while kinetics decide the reaction rate which is associated with charge transport (in the electrolyte and the active materials) and charge transfer (in two phase interface). To electric vehicles for example, the longest travel distance is determined by thermodynamics and the fastest travel speed relates to kinetics. The kinetics can be expressed by the following equations (eqs. 6–9 for batteries and eq. 10 for capacitors):^{16, 27, 28}

$$PD = E \times I \quad (6)$$

$$I = i_0 \left[\exp\left(\frac{\alpha F \eta}{RT}\right) - \exp\left(-\frac{(1-\alpha) F \eta}{RT}\right) \right] \quad (7)$$

$$i_0 = A \exp\left(-\frac{E_a}{RT}\right) \quad (8)$$

$$i_0 = \frac{RT}{nFR_{ct}} \quad (9)$$

$$PD = \frac{E^2}{4R_s} \quad (10)$$

where PD is the power density, I is the current, i_0 is the exchanging current, α is the transfer coefficient, η is the polarization, R is the gas constant, T is the absolute temperature, A is the temperature-independent coefficient, E_a is the apparent activation energies, R_{ct} is the charge transfer impedance, and R_s is the equivalent inner impedance. High power density needs large i_0 and effective mass transport, which means facile electronic conductivity and ionic diffusion (Fig. 2b). For batteries, nanosized electrode materials facilitate the improvement of kinetics due to the increased reaction interface and reduced diffusion path for ionic intercalation and deintercalation.^{2, 29–31} In general, the relationship among the ionic diffusion time (τ) in the host material, the ionic diffusion length (L_{ion}), and the ionic diffusion coefficient (D_{ion}) can be described as follows:¹⁸

$$\tau = \frac{L_{ion}^2}{D_{ion}} \quad (11)$$

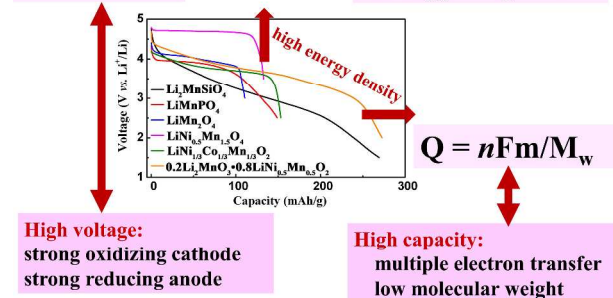
For similar D_{ion} , the τ increases proportionately with the square of the L_{ion} . In other words, the ionic diffusion time can reduce by two orders of magnitude when the ionic diffusion length is changed from 100 nm to 10 nm. Therefore, nanostructure benefits the complete utilization of the active materials at high current density (Fig. 2c). Among various nanostructures, one-dimensional (1D) nanostructures such as nanotubes, nanowires, and nanorods have received considerable interests because of their rapid electron transport along the 1D direction and short ionic diffusion distance along the radial direction.^{32–34} For pseudocapacitors, the limitations of ionic diffusion are removed, leading to high power density. Nanostructured materials shorten the electronic transport and ionic diffusion distance to further improve the rate performance.³⁵ However, nanostructured materials are plagued by low volumetric energy density owing to low tapping density and undesirable side reactions which are induced by their highly reactive surface. Recently, hierarchical micro-nano structure is an effective strategy to solve the problems, which can maintain the advantages of micromaterials and nanomaterials.^{36, 37}

In this review, recent efforts to use nanostructured Mn-based oxides for batteries and capacitors with high energy and power density are summarized. The synthetic method and applications of nanostructured Mn-based oxides in primary batteries, Li secondary batteries, metal–air batteries, and pseudocapacitors are introduced in the following sections. The relationship between nanostructure and electrochemical performance is discussed in detail. The challenges and perspectives of Mn-based oxides are proposed for further development in electrochemical energy storage and conversion.

(a) Thermodynamics

$$\Delta G = -nFE$$

$$\text{Energy} = Q \times E$$



(b) Kinetics

$$i = i_0 \left\{ \exp\left[\frac{\alpha F \eta}{RT}\right] - \exp\left[-\frac{(1-\alpha) F \eta}{RT}\right] \right\}$$

$$i_0 = A \exp\left(-\frac{E_a}{RT}\right)$$

$$i_0 = \frac{RT}{nFR_{ct}}$$

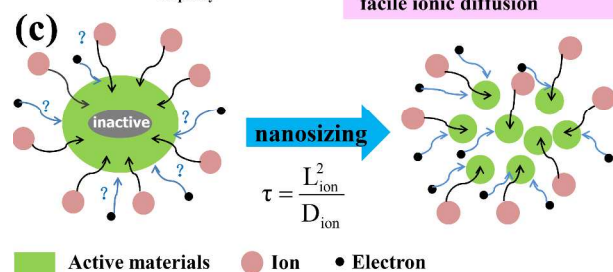
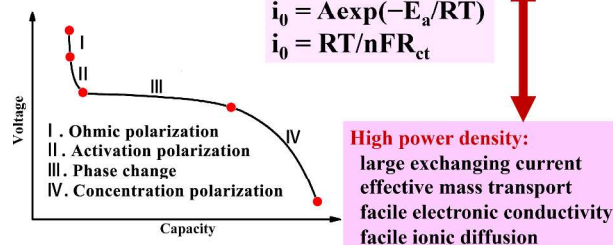


Fig. 2. Thermodynamics (a) and kinetics (b) basis of batteries. High energy density means strong oxidizing cathode and reducing anode as well as multiple electron reaction and low molecular weight of active materials. High power density means facile electronic conductivity and ionic diffusion. (c) Schematic illustration of electronic conduction and ionic transport within bulk counterparts and nanomaterials. Nanostructure can effectively improve the thermodynamics and kinetics.

2. MnO₂ as cathode materials for primary batteries

Primary batteries as facile and convenient chemical power sources have been widely applied to civil and military facilities such as flashlight, radio, and wristwatch. Primary batteries are fabricated in a “charged” state; while after discharging, primary batteries cannot be charged again. Typical primary batteries include primary Zn–MnO₂, Li–MnO₂, and Mg–MnO₂ batteries. MnO₂ is usually used as cathode materials. Table 1 summarizes the electrochemical reactions, potential, and discharge capacity of common primary batteries. The essential obstacle of primary batteries is their low utilization efficiency of the active materials, resulting in low practical capacity and large electrochemical polarization. The development of nanostructured materials offers an intriguing strategy to increase the discharge capacity and operating voltage of primary batteries.

MnO₂ can be obtained from nature, chemical synthesis (e.g., hydrothermal/solvothermal, sol-gel, template, deposition, and micro-lacteous methods), and electrochemical preparation (e.g.,

electrochemical reactions, electro-deposition, and electrospinning).^{7, 38–44} Table 2 summarizes the crystallographic structure, morphology, and synthesis method with the corresponding reaction equations of several nanostructured MnO₂. Facile hydrothermal methods were used to prepare the MnO₂ nanomaterials with 1D shapes (nanorods, nanowires, and nanotubes), 2D hierarchical forms (hexagramlike and

dendritelike), and 3D morphologies (flowerlike nanospheres). The γ -MnO₂ nanoflake, nanoneedle, and nanorod films were synthesized through convenient electrodeposition techniques. Hollow MnO₂ spheres and cubes were obtained by simple decomposition of MnCO₃ precursors.

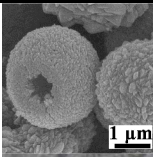
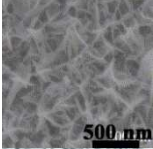
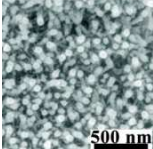
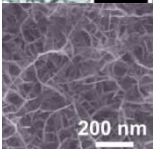
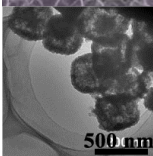
Table 1. Electrochemical reactions, potential, and discharge capacity of selected primary batteries.

Primary batteries	Reactions	Potential (V) ^a	Capacity (mAh/g) ^b	Ref.
Alkaline Zn–MnO ₂ batteries	(+) MnO ₂ + H ₂ O + e [−] → MnOOH + OH [−]	1.20	267	39
	(−) Zn → Zn ²⁺ + 2e [−]			
Li–MnO ₂ batteries	Overall: Zn + 2MnO ₂ + 2H ₂ O → 2MnOOH + Zn ²⁺ + 2OH [−]	2.65	>210	39
	(+) MnO ₂ + xLi ⁺ + xe [−] → Li _x MnO ₂			
	(−) Li → Li ⁺ + e [−]			
Mg–MnO ₂ batteries	Overall: xLi + MnO ₂ → Li _x MnO ₂	1.44	768	45
	(+) MnO ₂ + H ₂ O + e [−] → MnOOH + OH [−]			
	(−) Mg → Mg ²⁺ + 2e [−]			
Overall: Mg + 2MnO ₂ + 2H ₂ O → 2MnOOH + Mg ²⁺ + 2OH [−]				

^{a, b} The potentials and capacities are given by previous reports for metal–MnO₂ batteries.

Table 2. Crystallographic structure, morphology, and synthesis method with the corresponding reaction equations of several nanostructured MnO₂.

Structure	Morphology	Reaction equation	Method	Ref.
α -MnO ₂	nanowires	2KMnO ₄ + 3MnSO ₄ + 2H ₂ O → 5 α -MnO ₂ + K ₂ SO ₄ + 2H ₂ SO ₄	hydrothermal method	39
	flowerlike nanospheres			
β -MnO ₂	nanowires	Mn(NO ₃) ₂ → β -MnO ₂ + 2NO ₂ ↑ 4NO ₂ + O ₂ + 2H ₂ O → 4HNO ₃	hydrothermal method	39
	hexagonal starlike			
	dendritelike			
γ -MnO ₂	nanorods	MnSO ₄ + (NH ₄) ₂ S ₂ O ₈ + 2H ₂ O → γ -MnO ₂ + (NH ₄) ₂ SO ₄ + 2H ₂ SO ₄	hydrothermal method	39
	nanowires/nanotubes			
		[(MnSO ₄)(PEG-6000)(H ₂ O)] + O ₂ + OH [−] → γ -MnO ₂	PEG-assisted solvothermal method	11

	hollow spheres		$\text{MnSO}_4 + \text{NH}_4\text{HCO}_3 + 2\text{H}_2\text{O} \rightarrow \text{MnCO}_3\downarrow + \text{NH}_4\text{H}_2\text{SO}_4$ $\text{MnCO}_3 \rightarrow \gamma\text{-MnO}_2 + \text{CO}_2\uparrow$	hydrothermal method + calcination	40
$\gamma\text{-MnO}_2$ film	carambola-like nanoflake		$\text{Mn}^{2+} + 2\text{H}_2\text{O} \rightarrow \gamma\text{-MnO}_2 + 4\text{H}^+ + 2\text{e}^-$	electrodeposition technique	47
	nanorods				
$\varepsilon\text{-MnO}_2$	sponge-like nanostructure		$\text{Mn}^{2+} + 2\text{H}_2\text{O} \rightarrow \gamma\text{-MnO}_2 + 4\text{H}^+ + 2\text{e}^-$	electrodeposition technique	41
Amorphous MnO_2	hollow nanocubes		$2\text{NH}_4\text{HCO}_3 + \text{MnSO}_4 \rightarrow \text{MnCO}_3\downarrow + (\text{NH}_4)_2\text{SO}_4 + \text{CO}_2\uparrow + \text{H}_2\text{O}$ $3\text{MnCO}_3 + 2\text{KMnO}_4 \rightarrow 5\text{MnO}_2 + \text{K}_2\text{CO}_3 + 2\text{CO}_2\uparrow$	microemulsion method	48

2.1 Zn–MnO₂ batteries

Among various portable batteries, primary Zn–MnO₂ batteries accounted for about 90% of the total sales per year due to their low cost and environmental compatibility.⁴⁹ In 1860, Leclanché first reported the carbon–zinc battery using zinc foil as anode, natural MnO₂ and carbon black as cathode, and ZnCl₂–NH₄Cl (aq) as electrolyte. In the following hundred years, commercial Zn–MnO₂ batteries composed of a mixture of electrolytic MnO₂ and graphite cathode, Zn anode, and synthetic gel electrolyte are widely used. The discharge product of MnO₂ cathode is MnOOH, the theoretical capacity is 308 mAh g⁻¹, but practical capacity is usually less than 250 mAh g⁻¹. Increasing the utilization of the active materials is a supreme challenge of Zn–MnO₂ batteries. As the synthetic technology of nanomaterials develops, nanostructured MnO₂ has been attempted to solve the problem.^{11, 50}

The previous researches indicate that the electrochemical performance of MnO₂ is mainly related to three factors: crystallographic structure, crystalline size, and microcosmic morphology.^{11, 47} MnO₂ can form various structural forms such as α -, β -, γ -, δ -, and λ -type through different connection ways of the basic structural units (*i.e.*, MnO₆ octahedron). By changing the synthetic methods, particle size and morphology of MnO₂ cathode are controllable modified. Fig. 3 shows the crystal structures, reaction equations, and discharge curves of nanostructured and bulk MnO₂ prepared by our group.³⁹ For alkaline Zn–MnO₂ batteries, the discharge capacity decreases in the order of nano- γ > nano- α > bulk- γ >> nano- β . As shown in Figs. 3a–3c, α -, β -, and γ -MnO₂ respectively form (2×2), (1×1), and (1×2) tunnels via the different connection ways of MnO₆ octahedron. Large tunnel is favorable for ionic diffusion, so nanostructured γ - and α -MnO₂ deliver higher capacity than that of nanostructured β -MnO₂. However, the tunnels of α -MnO₂ usually contain impure cations and small molecules such as NH₄⁺, K⁺, or H₂O originated from the raw materials in the solution-based process. These impure cations and small molecules

stabilize the frame of α -MnO₂, but hamper the ionic diffusion and intercalation, leading to worse performance than that of nanostructured γ -MnO₂. The former reports have confirmed that various nanostructured MnO₂ electrodes show better performance than that of bulk MnO₂. Nanostructured γ -MnO₂ displayed a high discharge capacity of 267 mAh g⁻¹, but the capacity of bulk γ -MnO₂ was less than 150 mAh g⁻¹. Notably, the discharge capacity of nanostructured α -MnO₂ was even higher than that of the bulk γ -MnO₂. Nanostructured MnO₂ has high surface area, which ameliorates the effective contact between the active materials and the electrolyte, resulting in low internal resistance, fast proton diffusion, and high utilization efficiency.

Electrolytic technique is a common method to prepare nanostructured MnO₂ with different morphologies. The as-obtained thin film electrode avoids using the conducting and binding agents, which is in favor of study on the intrinsic properties of active materials. The γ -MnO₂ nanorod films delivered the highest discharge capacity of 269 mAh g⁻¹ due to their fascinating 1D nanostructure, while γ -MnO₂ nanoflake films displayed a high potential plateau (~1.0 V).⁴⁷ In addition, as MnO₂ is a semiconductor with poor electronic conductivity, conducting polymer coating is an effective strategy to enhance the conductivity.⁵¹

2.2 Li–MnO₂ batteries

Primary lithium batteries have also attracted a lot of interests because the molecular weight of lithium is the smallest among all metal elements. Unlike Zn–MnO₂ batteries, the electrolytes of Li–MnO₂ batteries are non-aqueous, and the discharge product of cathode is Li_{0.6}MnO₂. The effects of structure and morphology on the electrochemical performance of Li–MnO₂ batteries are also worth researching. α -MnO₂ possesses a hollandite-type structure with the (2×2) tunnel which facilitates the diffusion of Li⁺ ions. Hermann's group⁵² reported the preparation of α -MnO₂ nanofibers with 100 nm diameter by combining sol–gel route and template method, showing the discharge capacity of 183 mAh g⁻¹ that corresponds to the composition of Li_{0.6}MnO₂. Kijima *et al.*⁵³ synthesized Li-inserted α -

MnO₂ via soaking the α -MnO₂ powder in a mixed solution of LiOH and LiNO₃. Rietveld refinement determined that Li-inserted α -MnO₂ is (Li₂O)_{0.12}MnO₂ with the hollandite-type structure. (Li₂O)_{0.12}MnO₂ showed higher capacity and an average voltage than those of α -MnO₂. Our group prepared 1D α -MnO₂ nanostructures through a hydrothermal method. The discharge curve exhibits a flat plateau between 3.0 and 2.5 V with the capacity of 204.4 mAh g⁻¹ (Fig. 3e).

Nanostructured γ -MnO₂ can display a capacity of more than 210 mAh g⁻¹ in a Li-MnO₂ battery, but its average voltage is lower than α -MnO₂.³⁹ Bowden and co-authors synthesized Li-inserted γ -MnO₂ by heat treating the mixture of electrolytic γ -MnO₂ and LiOH. The Li-inserted γ -MnO₂ showed a capacity of around 210 mAh g⁻¹ and a discharge plateau of about 2.9 V. Some reports focused on the effects of heat treatment on electrochemical performance of electrolytic γ -MnO₂.^{54–57} It is found that heat treatment can change the cell volume, crystallite size, oxygen content, valance of Mn, and BET surface area of γ -MnO₂. Among these complex factors, high ratio of Mn(IV)/Mn(III) combined with a low (but non-zero) cation defects are very important to improve the capacity and plateau potential. Through heating under air at 400 °C, the treated MnO₂ delivered a high capacity of 266 mAh g⁻¹ at 5 mA g⁻¹.⁵⁶

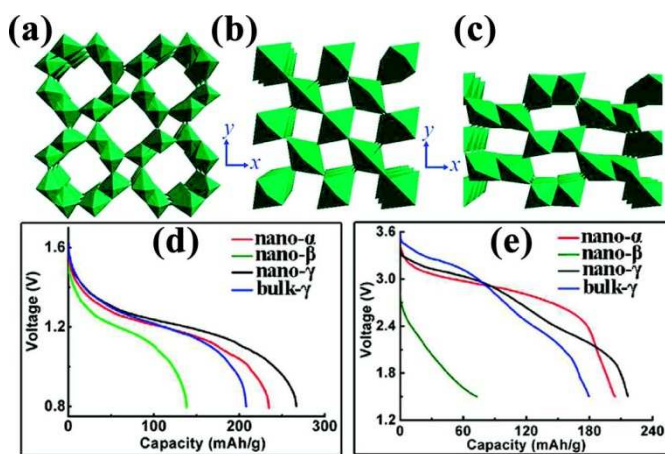


Fig. 3. Crystal structure of α -MnO₂ (a), β -MnO₂ (b), and γ -MnO₂ (c). The crystal structures are viewed along the z-axis. Discharge curves of bulk and nanostructured MnO₂ in Zn-MnO₂ (d) and Li-MnO₂ (e) batteries with the corresponding reaction equations. Reproduced with permission from ref. 17, Copyright 2009, American Chemical Society.

β -MnO₂ possesses very narrow (1×1) tunnels, which obstructs the diffusion of Li⁺ ions, leading to low potential and capacity. However, Bruce's group¹⁹ reported a high capacity (280 mAh g⁻¹) of ordered mesoporous β -MnO₂ prepared by template process. The performance was attributed to its high surface area and interconnected porous nanostructure. Doping with heteroatoms (e.g., Fe and V) is also an effective strategy to anisotropically change the lattice parameters of heat treated β -MnO₂, which enlarges the diffusion channel of Li⁺ ions.^{58, 59}

λ -MnO₂ can deliver a capacity of more than 220 mAh g⁻¹ with two plateaus of 4 V and 3 V, resulting in higher energy density than that of heat treated α -, β -, or γ -MnO₂.⁶⁰ However, λ -MnO₂ is usually prepared by etching out the Li of LiMn₂O₄ spinel, while LiMn₂O₄ is a cathode of LIBs. Preparing the electrode materials of primary batteries by using the electrode materials of secondary batteries as starting materials is uneconomical.

2.3 Mg-MnO₂ batteries

Mg-MnO₂ batteries are also aqueous primary batteries. Mg anode has a low redox potential (2.36 V vs. SHE) and high specific capacity (2.2 Ah g⁻¹), but the dense passivation film formed on the surface of Mg anode decreases the utilization and kinetics of Mg anode, leading to a high corrosion rate.⁴⁵ Using the nanostructured electrode materials with the modified electrolyte is an effective strategy to solve the problem. Mg-MnO₂ batteries composed of the γ -MnO₂ nanowires, Mg micro/nanospheres, and mixed electrolyte of Mg(NO₃)₂ and NaNO₂ display long discharge plateaus at 1.44 V and high specific discharge capacity of 768 mAh g⁻¹ because of the sufficient electrochemical contact and low electrode polarization.⁴⁵ For MnO₂ nanoparticles, shortening the particle size can increase the discharge capacity and energy density.⁶¹ The nanostructured MnO₂/graphene composites improve the conductivity, leading to better performance than bare MnO₂.⁶² The main problems of Mg-MnO₂ batteries focus on anode and electrolyte, the nanostructured MnO₂ only partially improve the performance.

3. Mn-based oxides as electrode materials for rechargeable Li-ion Batteries

Primary batteries cannot be recycled and random discard may cause environmental pollution. The rechargeable batteries can achieve the repeated conversion between electrical energy and stored chemical energy, which meet the stringent requirements for various electronic devices and large-scale electricity storage.^{5, 63} Among a wide variety of rechargeable batteries, LIBs dominate the rechargeable battery market segment.^{30, 64} However, present commercial LIBs based on LiCoO₂ cathode and graphite anode can hardly satisfy the demand of high energy and power density (i.e., high capacity, high voltage, and high-rate performance). Many Mn-based oxides are explored as the electrodes of LIBs. For example, Mn_xO_y can be reversibly cycled via the conversion reactions between manganese oxides and metallic Mn.^{40, 65} Spinel-type LiMn₂O₄ and LiNi_{0.5}Mn_{1.5}O₄ as cathode materials have also received a lot of interests because of their high discharge plateaus and fast ionic diffusion.^{13, 66} Layered manganese oxides as cathode materials have widely studied owing to their high theoretical capacity.^{67, 68} Polyanion-type Li₂MnSiO₄ achieves a 2e⁻ reaction with a theoretical capacity of 333 mAh g⁻¹.^{20, 69} Table 3 lists the electrochemical reactions, plateau potential, and theoretical capacity of Mn-base oxides as electrode materials of LIBs. These efforts demonstrate that manganese oxides are promising candidates in the applications for LIBs.

Table 3. Electrochemical reactions, potential, and discharge capacity of Mn-base oxides as electrode materials of LIBs.

Electrode materials	Reactions	Plateau potential (V)	Theoretical capacity (mAh/g)	Ref.
MnO ₂	MnO ₂ + 0.92Li ⁺ + 0.92e ⁻ ↔ Li _{0.92} MnO ₂ (2.0–4.5 V)	2.8	284	19
	MnO ₂ + 4Li ⁺ + 4e ⁻ ↔ Mn + 2Li ₂ O (0.02–3.3 V)	0.4	1233	40
Mn ₃ O ₄	Mn ₃ O ₄ + 8Li ⁺ + 8e ⁻ ↔ 3Mn + 4Li ₂ O	~0.4	936	70
MnO	MnO + 2Li ⁺ + 2e ⁻ ↔ Mn + Li ₂ O	<0.8	756	71

$o\text{-LiMnO}_2$	$\text{LiMnO}_2 \leftrightarrow \text{MnO}_2 + \text{Li}^+ + \text{e}^-$	~4.0 ~3.0	285	72
$\text{LiNi}_{0.5}\text{Mn}_{0.5}\text{O}_2$	$\text{LiNi}_{0.5}\text{Mn}_{0.5}\text{O}_2 \leftrightarrow \text{Ni}_{0.5}\text{Mn}_{0.5}\text{O}_2 + \text{Li}^+ + \text{e}^-$	3.8	280	73
$\text{LiNi}_{1/3}\text{Co}_{1/3}\text{Mn}_{1/3}\text{O}_2$	$\text{LiNi}_{1/3}\text{Co}_{1/3}\text{Mn}_{1/3}\text{O}_2 \leftrightarrow \text{Ni}_{1/3}\text{Co}_{1/3}\text{Mn}_{1/3}\text{O}_2 + \text{Li}^+ + \text{e}^-$	3.8	280	74
$\text{Li}(\text{Li}_{1/3-2x/3}\text{M}_x\text{Mn}_{2/3-x/3})\text{O}_2$	$\text{Li}(\text{Li}_{1/3-2x/3}\text{M}_x\text{Mn}_{2/3-x/3})\text{O}_2 \leftrightarrow \text{Li}_{1/3-2x/3}\text{M}_x\text{Mn}_{2/3-x/3}\text{O}_2 + \text{Li}^+ + \text{e}^-$	3.5–4.0	250–300	75
LiMn_2O_4	$\text{LiMn}_2\text{O}_4 \leftrightarrow \lambda\text{-MnO}_2 + \text{Li}^+ + \text{e}^-$	~4.0	148	13
$\text{LiNi}_{0.5}\text{Mn}_{1.5}\text{O}_4$	$\text{LiNi}_{0.5}\text{Mn}_{1.5}\text{O}_4 \leftrightarrow \text{Ni}_{0.5}\text{Mn}_{1.5}\text{O}_4 + \text{Li}^+ + \text{e}^-$	~4.7	147	66
LiMnPO_4	$\text{LiMnPO}_4 \leftrightarrow \text{MnPO}_4 + \text{Li}^+ + \text{e}^-$	4.1	171	76
$\text{Li}_2\text{MnSiO}_4$	$\text{Li}_2\text{MnSiO}_4 \leftrightarrow \text{MnSiO}_4 + 2\text{Li}^+ + 2\text{e}^-$	>3	333	20

3.1 Binary manganese oxides

In earlier researches, Li–MnO₂ primary batteries were attempted to become the Li–MnO₂ secondary batteries, but the discharge capacities rapidly fade because of the conversion from MnO₂ to LiMn₂O₄. The 1D nanostructure can slow the decay, but not stop the decay.³⁹ The ordered mesoporous structure not only accommodates the volume changes but also provides the diffusion channels of Li⁺ ions, which effectively improves the cycling and rate performance.¹⁹ Furthermore, the lithium dendrites may cause a security threat, which restricts the development of Li–MnO₂ batteries.

Various binary Mn-based oxides (*e.g.*, MnO₂, Mn₃O₄, and MnO) can serve as anode materials of LIBs based on electrochemical conversion reactions. Our group synthesized nanoporous γ -MnO₂ hollow nanocubes and microspheres via a hydrothermal route combined with thermal treatment.⁴⁰ The as-prepared γ -MnO₂ microspheres and nanocubes displayed the first discharge capacities of 1289.0 and 1992.6 mAh g⁻¹, respectively. After 20 cycles, the discharge capacities of γ -MnO₂ microspheres and nanocubes decayed to 602.1 and 656.5 mAh g⁻¹, respectively. The morphology and particle size have intensive effects on the reaction interface and electrochemical performance. The as-prepared γ -MnO₂ nanocubes have smaller particle size and larger surface area, leading to shorter diffusion distance of Li⁺ ions and more efficient contact with the conductive carbon and electrolyte.

Mn₃O₄ is also a potential anode material for LIBs, but its low electronic conductivity (~10⁻⁷–10⁻⁸ S cm⁻¹) and large volume change during the cycles restrain the capacity. Loading Mn₃O₄ nanoparticles on the reduced graphene oxide (rGO) is an effective approach to improve the capacity, rate capability, and cycling stability.⁷⁰ The Mn₃O₄-rGO composite showed discharge capacities of ~780 mAh g⁻¹ at 400 mA g⁻¹ and ~390 mAh g⁻¹ at 1600 mA g⁻¹. The high performance is attributed to highly conductive rGO which not only enhances the electronic conductivity but also restricts the growth and aggregation of Mn₃O₄ nanoparticles during the cycles.

MnO is one of widely studied anode materials but shares the same problems with Mn₃O₄. Designing nanofilms or nanoporous structure can accommodate the volume change, leading to improving cycling performance. The nanocrystalline MnO thin film displayed a discharge capacity of 425 mAh g⁻¹ at 0.125C after 25 cycles.⁷⁷ The porous MnO microspheres delivered a capacity of 800 mAh g⁻¹ at 50 mA g⁻¹ along with capacity retention of 88% after 50 cycles.⁷⁸ The porous MnO nanoflakes showed a high reversible capacity of 648 mAh g⁻¹ after 100 cycles at 246 mA g⁻¹.⁷⁹ Another common strategy is combining nanostructured MnO with conductive materials such as coaxial MnO/C nanotubes,⁸⁰ MnO/C core-shell nanorods,^{81, 82} MnO/rGO composite,⁸³ porous MnO/C disks,⁸⁴ and MnO@C core-shell nanoplates.⁸⁵ Nanostructured MnO/C composites gain improved conductivity, acceptable restricted volume change, and durable high-rate capability. MnO/C nanopeapods showed high capacities of 1119 mAh g⁻¹ at 500 mA g⁻¹ and 463 mAh g⁻¹ at 5000 mA g⁻¹ as well as no capacity fading and morphology change after

1000 cycles at 2000 mA g⁻¹ (Fig. 4).⁷¹ MnO/graphene hybrid anode exhibited high reversible capacity (2014 mAh g⁻¹ after 150 cycles at 200 mA g⁻¹), excellent long-term cyclability (843.3 mAh g⁻¹ after 400 cycles at 2000 mA g⁻¹) and superior high-rate capability (625.8 mAh g⁻¹ at 3000 mA g⁻¹).⁶⁵ Noticeably, MnO/C composites usually undergo a stage of capacity increase during the early cycles, and the reversible capacity is higher than the theoretical capacities of both MnO (756 mAh g⁻¹) and carbon (grapheme: 744 mAh g⁻¹ and graphite: 372 mAh g⁻¹) at low current density. It may be attributed to that Mn²⁺ are oxidized to a higher oxidation state,⁶⁵ but detailed reaction mechanism needs to be further studied.

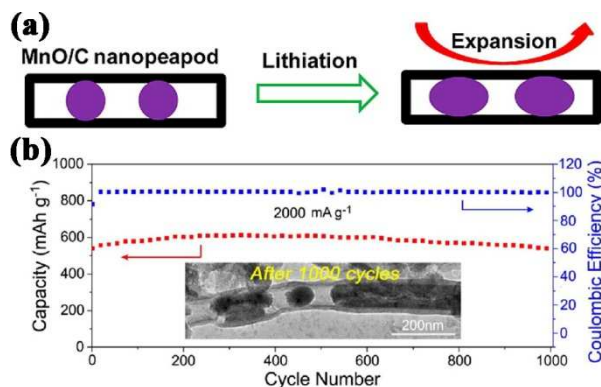


Fig. 4. (a) Schematic illustration: the MnO/C nanopeapods provide enough internal void space for accommodating the volume expansion of MnO during the cycles. (b) Cycling performance of the MnO/C nanopeapods at 2000 mA g⁻¹ for 1000 cycles (the inset showing the TEM image of MnO/C nanopeapods after over 1000 cycles). Reproduced with permission from ref. 71, Copyright 2014, American Chemical Society.

Though nanostructure binary Mn-based oxides improve the rate and cycling performance, but the high capacity is only obtained during charge to 3 V. As known, because anode materials need low charge plateaus, binary Mn-based oxides are difficult to meet this requirement. Recently, many attentions have focused on Mn-based composite oxides.

3.2 Layered Mn-based oxides

LiCoO₂ as the first commercial cathode material of LIBs has an ordered layered structure with R $\bar{3}m$ space group. LiCoO₂ has high theoretical capacity of 274 mAh g⁻¹ and plateau potential of 3.9 V, but the practical capacity is only ~140 mAh g⁻¹.⁸⁶ Furthermore, LiCoO₂ suffers from high price and safety hazards. Although layered LiMnO₂ has high practical capacity of ~200 mAh g⁻¹ and low cost, it is difficult to be synthesized because of the inferior thermodynamic stability, which also hinders its practical commercialization.⁸⁶ In addition, Jahn–Teller distortion of Mn³⁺ can cause the phase conversion and

disproportionation reaction of Mn^{3+} leads to the manganese dissolution. Layered Mn-based oxides are also plagued by oxygen evolution at high charging potential to cause serious safety issues. Orthorhombic LiMnO_2 ($o\text{-LiMnO}_2$) with Pmm symmetry is also attempted as cathode for LIBs owing to its high theoretical capacity $\sim 285 \text{ mAh g}^{-1}$.⁷² However, $o\text{-LiMnO}_2$ easily transforms to a spinel-like phase during charge-discharge process, leading to awful cyclability. To solve these problems, nanostructured $\text{LiNi}_{0.5}\text{Mn}_{0.5}\text{O}_2$, $\text{LiNi}_{1/3}\text{Co}_{1/3}\text{Mn}_{1/3}\text{O}_2$, and Li-rich phase Li-rich $\text{Li}(\text{Li}_{1/3-2x/3}\text{M}_x\text{Mn}_{2/3-x/3})\text{O}_2$ are proposed.

3.2.1 Layered $\text{LiNi}_x\text{Mn}_{1-x}\text{O}_2$

Ni and Mn cations can appear randomly in transition metal layers with all ratios to form a $\text{LiNi}_x\text{Mn}_{1-x}\text{O}_2$ solid solution. When $x \geq 0.5$, the solid solution shows a hexagonal $\alpha\text{-NaFeO}_2$ structure, while when $x < 0.5$, the spinel structure is formed by reconstitution reactions.⁸⁶ In 1992, Dahn's group studied the structure and electrochemistry of the solid-solution series $\text{Li}_y\text{Ni}_x\text{Mn}_{1-x}\text{O}_2$ ($0.5 < x < 1$ and y near 1).⁸⁷ The results showed that the reversibly capacity decreased with the increase of x . After that, Ohzuku *et al.* systematically investigated $\text{LiNi}_{0.5}\text{Mn}_{0.5}\text{O}_2$ cathode which delivered a discharge capacity of $\sim 200 \text{ mAh g}^{-1}$ with a plateau potential of 3.8 V.⁸⁸ $\text{LiNi}_{0.5}\text{Mn}_{0.5}\text{O}_2$ is layered-hexagonal structure with R $\bar{3}m$ symmetry, and Li^+ , Ni^{2+} , and Mn^{4+} are arranged in the lithium layer and transition metal layer. During cycling, the redox reaction involves a change from Ni^{2+} to Ni^{4+} , whereas the Mn^{4+} remains, which avoids the Jahn–Teller distortions of Mn^{3+} .⁸⁹ However, about 10% Ni and Li ions may exchange in the lithium and transition metal layers,⁹⁰ leading to sluggish ionic diffusion. The rate capability of $\text{LiNi}_{0.5}\text{Mn}_{0.5}\text{O}_2$ can be improved by modifying the surface,⁹¹ adjusting the ratio of Ni and Mn,⁷³ and synthesizing the nanostructure.^{92, 93} Sun *et al.*⁹¹ prepared AlF_3 coated $\text{LiNi}_{0.5}\text{Mn}_{0.5}\text{O}_2$ which displayed better rate performance and thermal stability than bare $\text{LiNi}_{0.5}\text{Mn}_{0.5}\text{O}_2$. The results showed that the $\sim 10 \text{ nm}$ AlF_3 layer effectively reduced Ni and Mn dissolution and inhibited the decomposition of organic electrolyte. Liu and co-workers synthesized $\text{LiNi}_{0.5}\text{Mn}_{0.5}\text{O}_2$ nanosheets by using the flower-like MnO_2 nanosheets as a precursor.⁹² An initial discharge capacity of 162 mAh g^{-1} was exhibited at 0.6C, with a retention of 100% after 100 cycles, which illustrated that the two-dimensional (2D) nanostructure facilitated fast Li-intercalation/deintercalation kinetics and structural stability. Park and co-authors⁹⁴ fabricated lithium-deficient $\text{Li}_x\text{Mn}_{0.67}\text{Ni}_{0.33}\text{O}_2$ nanowires by hydrothermal method using the $\text{LiMn}_{0.5}\text{Ni}_{0.5}\text{O}_2$ powder as precursor. The $\text{Li}_x\text{Mn}_{0.67}\text{Ni}_{0.33}\text{O}_2$ nanowires delivered a reversible capacity of $\sim 230 \text{ mAh g}^{-1}$ at 20 mA g^{-1} owing to their 1D nanostructure.

3.2.2 Layered $\text{LiNi}_{1-x-y}\text{Co}_y\text{Mn}_x\text{O}_2$

Ternary transition metal oxide, $\text{LiNi}_{1-x-y}\text{Co}_y\text{Mn}_x\text{O}_2$, potentially combines the advantages of LiCoO_2 , LiNiO_2 , and $\text{LiNi}_{0.5}\text{Mn}_{0.5}\text{O}_2$ to achieve a practical capacity of $\sim 210 \text{ mAh g}^{-1}$. Though the values of x and y can be adjusted in a wide range, most reports were focused on two series of ternary transition metal oxides (*i.e.*, $\text{LiNi}_x\text{Mn}_x\text{Co}_{1-2x}\text{O}_2$ ($0 \leq x \leq 0.5$) and $\text{LiNi}_{1-2x}\text{Co}_x\text{Mn}_x\text{O}_2$ ($0 \leq x \leq 1/3$)). Whittingham's group⁹⁵ reported a systematic study of the rate and cycling performance of $\text{LiNi}_x\text{Mn}_x\text{Co}_{1-2x}\text{O}_2$ ($x = 0.5, 0.45, 0.4, \text{ and } 1/3$). The $\text{LiNi}_{1/3}\text{Mn}_{1/3}\text{Co}_{1/3}\text{O}_2$ delivered the highest capacity at high current density of 3 mA cm^{-2} , and the $\text{LiNi}_{0.4}\text{Mn}_{0.4}\text{Co}_{0.2}\text{O}_2$ exhibited comparable performance and lower cost. For $\text{LiNi}_{1-2x}\text{Co}_x\text{Mn}_x\text{O}_2$ cathode materials, Ni-rich layered $\text{LiNi}_{0.8}\text{Co}_{0.1}\text{Mn}_{0.1}\text{O}_2$ composed of Ni^{3+} , Co^{3+} , and Mn^{3+} displays

the highest capacity, but suffers from poor cycling performance owing to the structural transformation.⁹⁶ To exert synergistic effects of several $\text{LiNi}_{1-x-y}\text{Co}_y\text{Mn}_x\text{O}_2$ materials, core-shell structure using core material with high capacity and shell material with high stability is attempted. Sun *et al.*⁹⁷ reported a spherical core-shell structure with a $\text{LiNi}_{0.8}\text{Co}_{0.1}\text{Mn}_{0.1}\text{O}_2$ core and a $\text{LiNi}_{0.5}\text{Mn}_{0.5}\text{O}_2$ shell which delivered superior cyclability and thermal stability at 1C for 500 cycles. Then, Sun's group⁹⁸ designed a concentration-gradient cathode material with a $\text{LiNi}_{0.8}\text{Co}_{0.1}\text{Mn}_{0.1}\text{O}_2$ core, a $\text{LiNi}_{0.8-x}\text{Co}_{0.1+y}\text{Mn}_{0.1+z}\text{O}_2$ ($0 \leq x \leq 0.34$, $0 \leq y \leq 0.13$, and $0 \leq z \leq 0.21$) outer layer, and a $\text{LiNi}_{0.46}\text{Co}_{0.23}\text{Mn}_{0.31}\text{O}_2$ surface. The concentration-gradient cathode material exhibited a high capacity of 209 mAh g^{-1} at 0.5C with the capacity retention of 96% after 50 cycles.

Meanwhile, $\text{LiNi}_{1/3}\text{Co}_{1/3}\text{Mn}_{1/3}\text{O}_2$ which is proposed by Ohzuku *et al.*⁹⁹ has been also investigated extensively. $\text{LiNi}_{1/3}\text{Co}_{1/3}\text{Mn}_{1/3}\text{O}_2$ possesses an O3 type layered structure with a superlattice based on $[\sqrt{3} \times \sqrt{3}]R30\text{-type}$ in Wood's notation, resulting in a more stable structure than the basic layered oxides such as LiCoO_2 , LiNiO_2 , and LiMnO_2 .¹⁰⁰ The performance of $\text{LiNi}_{1/3}\text{Co}_{1/3}\text{Mn}_{1/3}\text{O}_2$ can be improved by manufacturing the nanostructure,^{74, 101, 102} adjusting the surface,^{103–105} doping other cations.^{106, 107} Nanostructured $\text{LiNi}_{1/3}\text{Co}_{1/3}\text{Mn}_{1/3}\text{O}_2$, which is usually prepared by co-precipitation with further heat treatment, can facilitate Li^+ ions intercalation/deintercalation process to obviously improve rate performance. The $\text{LiNi}_{1/3}\text{Co}_{1/3}\text{Mn}_{1/3}\text{O}_2$ hexagonal nanobricks with a high percentage of exposed $\{010\}$ facets showed $\sim 130 \text{ mAh g}^{-1}$ at 15C.¹⁰⁸ The cycle performance and thermal stability can be enhanced by surface coating. Li's group¹⁰⁹ prepared a series of 1D layered Mn-based oxides nanobelts, which exhibited impressive performance benefiting from the surface- Li_2TiO_3 -rich coating layer.

3.2.3 Layered Li-rich $\text{Li}(\text{Li}_{1/3-2x/3}\text{M}_x\text{Mn}_{2/3-x/3})\text{O}_2$

Though many efforts have been performed to improve the performance of Li-stoichiometric layered Mn-based oxides, the capacity is very difficult to exceed 220 mAh g^{-1} . Recently, Li-rich layered $\text{Li}(\text{Li}_{1/3-2x/3}\text{M}_x\text{Mn}_{2/3-x/3})\text{O}_2$ ($\text{M} = \text{Ni, Mn}$) has been proposed because of its initial discharge capacity of 300 mAh g^{-1} and reversible capacity of $\sim 250 \text{ mAh g}^{-1}$.^{67, 75, 110, 111} The Li-rich layered Mn-based oxides are designed based on Li_2MnO_3 which has a layered monoclinic structure with C2/m symmetry. The Li-rich layered Mn-based oxides are represented as a solid solution of the Li_2MnO_3 and Li-stoichiometric layered Mn-based oxides, so they can also be expressed as $x\text{Li}_2\text{MnO}_3 \cdot (1-x)\text{LiM}_{1-y}\text{Mn}_y\text{O}_2$. The Li-rich layered Mn-based oxides suffer from large initial irreversible capacity, phase transformation during the cycles, and poor rate performance. To solve these problems, many nanostructures have been attempted.^{111–114} Cho's group^{113, 115} prepared $\text{Li}_{0.88}(\text{Li}_{0.18}\text{Co}_{0.33}\text{Mn}_{0.49})\text{O}_2$ and $\text{Li}(\text{Li}_{0.15}\text{Ni}_{0.25}\text{Mn}_{0.6})\text{O}_2$ nanowires by hydrothermal method using $\text{Co}_{0.4}\text{Mn}_{0.6}\text{O}_2$ and $\text{Ni}_{0.3}\text{Mn}_{0.7}\text{O}_2$ as precursors, respectively. The $\text{Li}_{0.88}(\text{Li}_{0.18}\text{Co}_{0.33}\text{Mn}_{0.49})\text{O}_2$ nanowires exhibited a reversible capacity of 230 mAh g^{-1} at 3600 mA g^{-1} (15C) and $\text{Li}(\text{Li}_{0.15}\text{Ni}_{0.25}\text{Mn}_{0.6})\text{O}_2$ nanowires showed a discharge capacity of 311 mAh g^{-1} at 0.3C with capacity retention of 95% after 80 cycles. Jiang *et al.*¹¹⁶ fabricated nanocrystal-assembled hollow $0.3\text{Li}_2\text{MnO}_3 \cdot 0.7\text{LiNi}_{0.5}\text{Mn}_{0.5}\text{O}_2$ microspheres by template route. The as-obtained hollow spheres displayed a high reversible capacity of 295 mAh g^{-1} after 100 cycles. Our group¹¹¹ synthesized porous $0.2\text{Li}_2\text{MnO}_3 \cdot 0.8\text{LiNi}_{0.5}\text{Mn}_{0.5}\text{O}_2$ nanorods

assembled with nanoparticles through a solid-state reaction by using LiOH, Ni(NO₃)₂, and porous Mn₂O₃ nanowires as starting materials. As shown in Fig. 5, an initial discharge capacity of 275 mAh g⁻¹ was delivered at 0.2 C, with a capacity decay of ~10% after 100 cycles. The good performance was attributed to the porous 1D nanostructure which not only accommodated the intrinsic volume change but also reduced the diffusion distance of Li⁺ ions. Surface modification is also an effective mean to decrease the first irreversible capacity and improve the rate capability. Manthiram's group reported a series of functional surface modifications for Li-rich layered Li(Li_{1/3-2x/3}Ni_xMn_{2/3-x/3})O₂ such as Al₂O₃, RuO₂, AlPO₄ and CoPO₄.^{117, 118} The coating of Li(Li_{0.2}Mn_{0.54}Ni_{0.13}Co_{0.13})O₂ with 1 wt.% Al₂O₃ and 1 wt.% RuO₂ exhibited a high capacity of 280 mAh g⁻¹ at 0.05C and a capacity retention of 94.3% after 30 cycles.¹¹⁷

Large initial irreversible capacity, sluggish Li⁺ ion diffusion, and poor cycling stability are the main problems of layered Mn-based oxides. Nanostructures such as nanoparticles, nanorods, nanosheets, hollow structure, porous structure, and core-shell structure can enhance the rate and cycling performance. Table 4 lists the synthetic method, discharge capacity, cyclability, and rate capability of several nanostructured layered Mn-base oxides. From Table 4, it is difficult to obtain high capacity at large current rate (> 10C) and the capacity retention is relatively low after over 100 cycles. The surface coating with oxides, fluorides, and phosphates can reduce the surface reactivity to effectively improve the initial coulombic efficiency and cycle life, but it cannot absolutely avoid their internal phase transformation. Doping with other elements may promote the structure stability, but it is a challenge for the synthetic method.

Therefore, combination of spinel-type with high working potential and rate performance and polyanion-type Mn-based oxides with high specific capacity and thermal stability is proposed.

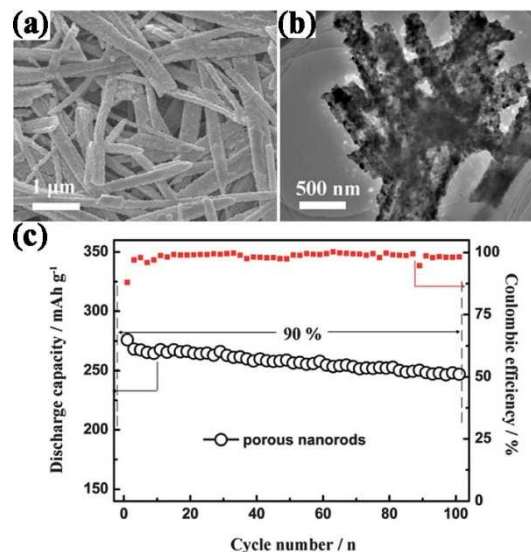


Fig. 5. SEM (a) and TEM (b) images of porous 0.2Li₂MnO₃·0.8LiNi_{0.5}Mn_{0.5}O₂ nanorods. (c) Cycling performance of 0.2Li₂MnO₃·0.8LiNi_{0.5}Mn_{0.5}O₂ nanorods at 0.2 C between 2.0 and 4.8 V. Reproduced with permission from ref. 111, Copyright 2014, The Royal Society of Chemistry.

Table 4. Synthetic method, discharge capacity, cyclability, and rate capability of several nanostructured layered Mn-base oxides as cathode materials of LIBs.

Materials	Synthetic method	Discharge capacity	Capacity retention	Rate capability	Ref.
Nanostructured LiNi _{0.5} Mn _{0.5} O ₂ spheres	Solid state reaction (γ-MnO ₂ hollow nanospheres as a precursor)	165 mAh g ⁻¹ at 36 mA g ⁻¹	93% after 75 cycles at 36 mA g ⁻¹	122 mAh g ⁻¹ at 576 mA g ⁻¹	93
LiNi _{0.5} Mn _{0.5} O ₂ nanosheets	Solid state reaction (flower-like MnO ₂ nanosheets as a precursor)	162 mAh g ⁻¹ at 108 mA g ⁻¹	100% after 100 cycles at 108 mA g ⁻¹	-	92
Li _x Mn _{0.67} Ni _{0.33} O ₂ (0.2 < x < 0.33) nanowires	Hydrothermal method (LiMn _{0.5} Ni _{0.5} O ₂ powder as a precursor)	~300 mAh g ⁻¹ at 20 mA g ⁻¹	80% after 12 cycles at 20 mA g ⁻¹	-	94
LiNi _{1/3} Co _{1/3} Mn _{1/3} O ₂ nanoparticles	Co-precipitation method	166 mAh g ⁻¹ at 40 mA g ⁻¹	95.5% after 50 cycles at 40 mA g ⁻¹	114 mAh g ⁻¹ at 800 mA g ⁻¹	101
Hollow LiNi _{1/3} Co _{1/3} Mn _{1/3} O ₂ spheres assembled with nanoparticles	Template method	175 mAh g ⁻¹ at 34 mA g ⁻¹	-	92 mAh g ⁻¹ at 1.7 A g ⁻¹	102
H ₃ PO ₄ modified porous LiNi _{1/3} Co _{1/3} Mn _{1/3} O ₂	Co-precipitation method	188.4 mAh g ⁻¹ at 0.1C	-	~100 mAh g ⁻¹ at 5C	103
LiNi _{1/3} Co _{1/3} Mn _{1/3} O ₂ nanobricks with a high percentage of exposed {010} facets	Co-precipitation method	179 mAh g ⁻¹ at 1C	89% after 100 cycles at 2C	130 mAh g ⁻¹ at 15C	108
Li(Li _{0.15} Ni _{0.25} Mn _{0.6})O ₂ nanowires	Solid state reaction (Ni _{0.3} Mn _{0.7} O ₂ as a precursor)	311 mAh g ⁻¹ at 120 mA g ⁻¹	95% after 80 cycles at 120 mA g ⁻¹	256 mAh g ⁻¹ at 2.8 A g ⁻¹	113
Li _{0.93} (Li _{0.21} Co _{0.28} Mn _{0.51})O ₂ nanoparticles	Hydrothermal method (Co _{0.35} Mn _{0.65} O ₂ as a precursor)	258 mAh g ⁻¹ at 25 mA g ⁻¹	95% after 30 cycles at 25 mA g ⁻¹	217 mAh g ⁻¹ at 1.0 A g ⁻¹	112

$\text{Li}_{0.88}(\text{Li}_{0.18}\text{Co}_{0.33}\text{Mn}_{0.49})\text{O}_2$ nanowires	Hydrothermal method ($\text{Co}_{0.4}\text{Mn}_{0.6}\text{O}_2$ nanowires as a precursor)	245 mAh g^{-1} at 48 mA g^{-1}	92% after 50 cycles at 240 mA g^{-1}	225 mAh g^{-1} at 3.6 A g^{-1}	115
Hollow $0.3\text{Li}_2\text{MnO}_3 \cdot 0.7\text{LiNi}_{0.5}\text{Mn}_{0.5}\text{O}_2$ spheres	Solid state reaction (porous MnO_2 spheres as a precursor)	295 mAh g^{-1} at 15 mA g^{-1}	94% after 100 cycles at 200 mA g^{-1}	172 mAh g^{-1} at 500 mA g^{-1}	116
Porous $0.2\text{Li}_2\text{MnO}_3 \cdot 0.8\text{LiNi}_{0.5}\text{Mn}_{0.5}\text{O}_2$ nanorods assembled with nanoparticles	Solid state reaction (porous Mn_2O_3 nanowires as a precursor)	275 mAh g^{-1} at 50 mA g^{-1}	90% after 100 cycles at 50 mA g^{-1}	192 mAh g^{-1} at 1.25 A g^{-1}	111
$0.5\text{Li}_2\text{MnO}_3 \cdot 0.5\text{LiNi}_{1/3}\text{Co}_{1/3}\text{Mn}_{1/3}\text{O}_2$ nanomaterials	Molten-salt strategy	313 mAh g^{-1} at 20 mA g^{-1}	70% after 100 cycles at 200 mA g^{-1}	197 mAh g^{-1} at 1.2 A g^{-1}	114
Core-shell structure ($\text{LiNi}_{0.8}\text{Co}_{0.1}\text{Mn}_{0.1}\text{O}_2$ as the core and $\text{LiNi}_{0.5}\text{Mn}_{0.5}\text{O}_2$ as the shell)	Co-precipitation method	200 mAh g^{-1} at 40 mA g^{-1}	98% after 500 cycles at 138 mA g^{-1}	~ 120 mAh g^{-1} at 138 mA g^{-1}	97
Concentration-gradient structure ($\text{LiNi}_{0.8}\text{Co}_{0.1}\text{Mn}_{0.1}\text{O}_2$ as the core, $\text{LiNi}_{0.8-x}\text{Co}_{0.1+y}\text{Mn}_{0.1+z}\text{O}_2$ ($0 \leq x \leq 0.34$, $0 \leq y \leq 0.13$, and $0 \leq z \leq 0.21$) as the outer layer, and $\text{LiNi}_{0.46}\text{Co}_{0.23}\text{Mn}_{0.31}\text{O}_2$ as the surface)	Co-precipitation method	209 mAh g^{-1} at 95 mA g^{-1}	96% after 50 cycles at 95 mA g^{-1}	-	98

3.3 Spinel-type Mn-based oxides

Spinel-type Mn-based oxides mainly include LiMn_2O_4 and $\text{LiNi}_{0.5}\text{Mn}_{1.5}\text{O}_4$. Though the theoretical specific capacity of spinel-type Mn-based oxides is lower than those of layered Mn-based oxides, their rate performance is outstanding. Spinel-type Mn-based oxides may become ideal cathode materials of power batteries.

3.3.1 Spinel-type LiMn_2O_4

As an appealing cathode material which offers high power capability and excellent safety, spinel LiMn_2O_4 has been exhaustively studied in the last 30 years. In the early 1980s, Thackeray *et al.* discovered that the $[\text{B}_2]\text{X}_4$ framework of many stable $\text{A}[\text{B}_2]\text{X}_4$ spinels can provide a stable host structure for the electrochemical insertion and extraction of lithium.^{119, 120} Ohzuku *et al.*¹²¹ studied the electrochemistry of spinel-related manganese dioxide in lithium nonaqueous cell, which proposed the classic reaction mechanism of $\text{Li}_x\text{Mn}_2\text{O}_4$ ($0 < x < 2$) during lithium insertion process. Later, Tarascon *et al.* successfully applied LiMn_2O_4 as the cathode in rechargeable rocking-chair batteries based on carbon anode. Such batteries show the advantages of long cycling life, high average open circuit voltage of 3.7 V, high power and low cost, being widely used in various areas.^{122, 123}

LiMn_2O_4 is a cubic spinel with space symmetry $\text{Fd}\bar{3}\text{m}$. The oxygen ions are cubic close packed in the 32e positions. The manganese ions are located on the 16d octahedral sites, while the lithium ions are positioned on the 8a tetrahedral sites. The MnO_6 octahedral in the spinel structure are edge-shared and form a continuous 3D cubic array, thus resulting in a robust Mn_2O_4 spinel framework. The 8a tetrahedral share each of their four faces with neighboring vacant 16c octahedral. During lithium extraction process, the lithium ions could move from one 8a site into another 8a site via adjacent 16c site in three different directions.¹²⁴ Lithium extraction occurs at approximately 4 V (vs. Li^+/Li) in a two-stage process ($\text{LiMn}_2\text{O}_4/\text{Li}_{0.5}\text{Mn}_2\text{O}_4$ and $\text{Li}_{0.5}\text{Mn}_2\text{O}_4/\lambda\text{-MnO}_2$) with 150 mV voltage difference. The high voltage stage was ascribed to the two phase reaction caused by lithium ion ordering on the 8a sites,

and the low voltage stage was ascribed to a homogeneous phase reaction. Further lithiation of LiMn_2O_4 occurs around 3 V, which leads to the formation of rock salt phase $\text{Li}_2\text{Mn}_2\text{O}_4$.¹²¹ During the lithium insertion/extraction reaction at 4 V, the unit cell contracts and expands by 7.6%. Nevertheless, the cubic symmetry of $\text{Li}_x\text{Mn}_2\text{O}_4$ is not affected, and the Mn_2O_4 framework could stay safe and sound. However, during the lithium insertion/extraction reaction at 3 V, the lithium ions are forced to fill the 16c sites, leading to the transition of spinel phase to rock salt phase. Meanwhile, the average oxidation stage of the manganese ions is less than 3.5, which would induce the Jahn-Teller distortion from cubic to tetragonal phase. The electrochemical performance of LiMn_2O_4 is deeply affected by its structural characteristics. The robust Mn_2O_4 framework with 3D lithium ion diffusion passways endows LiMn_2O_4 with promising safety and high rate capability. On the other side, the existence of Mn^{3+} leads to the manganese dissolution via a disproportionation reaction ($2\text{Mn}^{3+} \rightarrow \text{Mn}^{2+} + \text{Mn}^{4+}$), which hinders the cycle stability.¹²⁵⁻¹²⁷

At the expense of compromising the theoretical capacity, strategies proposed to improve the cycling stability of LiMn_2O_4 include surface coating and cation doping.¹²⁸⁻¹³¹ Recent approaches to enhance the cyclability and high-rate capability of LiMn_2O_4 cathode have been focused on constructing nanostructure.¹³²⁻¹³⁵ For example, porous LiMn_2O_4 nanograins, mesoporous Li-Mn-O spinels and LiMn_2O_4 hierarchical porous architectures showed better capacity retention than bulk counterpart without porosity. 1D nanostructures are also particularly attractive because they not only have large specific surface area which allows for efficient active mass-electrolyte contact but also provides 1D electron transport pathways. Previous works have proved that LiMn_2O_4 nanorods and nanotubes can exhibit remarkable high-rate capabilities.¹³⁶ Herein, it could be envisioned that 1D nanoporous spinel would combine the advantages of both 1D nanostructures and porous morphology. However, it remains a challenge to simultaneously obtain porosity and 1D nanostructure for LiMn_2O_4 , which adopts the cubic crystallographic structure and is unfavourable for anisotropic crystal growth along a 1D direction.

Our group prepared porous LiMn_2O_4 nanorods through solid state lithiation of 1D nanoporous Mn_2O_3 template.¹³ Fig. 6 displays the synthesis route, crystal structure, SEM image, and cycling performance of porous LiMn_2O_4 nanorods. The synthesis of porous Mn_2O_3 nanorods was achieved by thermal decomposition of the MnC_2O_4 rods precursor which resulted from precipitation of $\text{Mn}(\text{NO}_3)_2$ and $\text{H}_2\text{C}_2\text{O}_4$ in a confined microemulsion system. The formation of 1D structure could be attributed to the microemulsion which confines the nucleation speed and directs anisotropic crystal growth. The nanorods consisted of aggregated nanoparticles with size of approximately 20 nm. The discharge capacity of porous LiMn_2O_4 nanorods exceeded 80 mAh g^{-1} at 30C, and the capacity retention approached 90% up to 500 cycles at 2C. The lithium diffusion coefficient (D_{Li}) of the porous nanorods was $1.3 \times 10^{-8} \text{ cm}^2 \text{ s}^{-1}$. The result indicates that the spinel porous nanorods favour faster Li-ion intercalation kinetics. Besides, the interconnected pores favour electrolyte immersing and transportation, which could avoid partial overdischarge and thus improve the cycling life.

Other nanostructures are also attempted for LiMn_2O_4 .^{137–142} Bruce's group¹³⁷ synthesized porous nano- LiMn_2O_4 spinel by a one-pot resorcinol-formaldehyde route. The initial capacity reached 131 mAh g^{-1} and remained 118 mAh g^{-1} after 200 cycles at 0.5C. Cui's group¹³³ prepared LiMn_2O_4 nanorods via a solid-state reaction using $\beta\text{-MnO}_2$ nanorods. The nanorods delivered a capacity of 100 mAh g^{-1} at 1C with capacity retention of 85% after 100 cycles. Bak *et al.*¹⁴² fabricated $\text{LiMn}_2\text{O}_4/\text{rGO}$ nanocomposites by microwave-assisted hydrothermal method. The composites exhibited high specific capacities of 137 mAh g^{-1} at 1C, 117 mAh g^{-1} at 50C, and 101 mAh g^{-1} at 100C, respectively. Cho's group¹⁴³ demonstrated that the carbon-coated LiMn_2O_4 clusters consisting of many single-crystal nanoparticles possessed ultrahigh-rate capability. The sample exhibited a gravimetric energy density of 300 Wh kg^{-1} at a power density of 45 kW kg^{-1} and a volumetric energy density of 440 Wh L^{-1} at a power density of 68 kW L^{-1} .

Another issue of spinel LiMn_2O_4 is poor performance at high temperature ($\geq 40 \text{ }^\circ\text{C}$) because of the accelerating Mn dissolution. In order to solve the problem, some strategies such as surface coating and cation doping are proposed.^{144, 145} Surface coating would avoid direct contact between the electrolyte and LiMn_2O_4 , and cation doping can keep high content of Mn^{4+} to improve the structure stability induced. Cho's group¹⁴⁴ prepared AlPO_4 -coated $\text{Li}_{1.09}\text{Mn}_{1.83}\text{Al}_{0.08}\text{O}_4$ via a solid-state reaction combined with a solution-based coating method. The cathodes delivered an initial discharge capacity of 108 mAh g^{-1} and a capacity retention of 78% after 200 cycles at 0.5C under $60 \text{ }^\circ\text{C}$ without swelling problem.

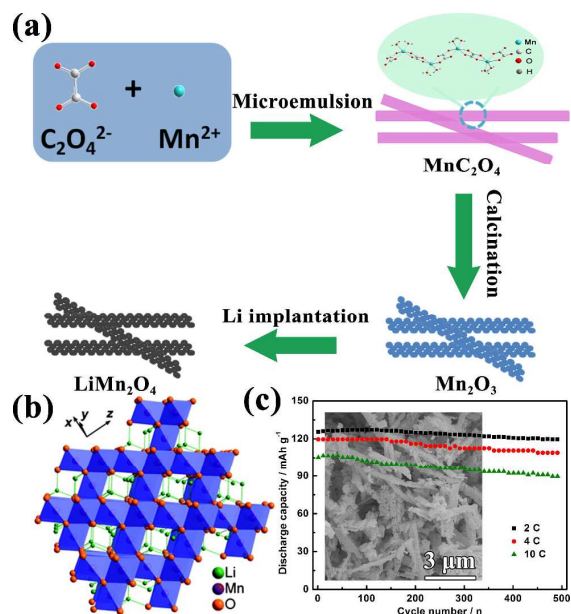


Fig. 6. (a) Schematic illustration of the synthesis, (b) Crystal structure, and (c) cycling performance of the porous LiMn_2O_4 nanorods at different discharge rates (the inset is the SEM image of the porous nanorods). Reproduced with permission from ref. 13, Copyright 2011, The Royal Society of Chemistry.

3.3.2 Spinel-type $\text{LiNi}_{0.5}\text{Mn}_{1.5}\text{O}_4$

Nickel substituted spinel LiMn_2O_4 was initially synthesized and studied as one of the metal substituted LiMn_2O_4 derivatives to increase the mean oxidation state of the manganese ions with a stable structure.^{146, 147} In spinel $\text{LiNi}_{0.5}\text{Mn}_{1.5}\text{O}_4$ (LNMO), sufficient Ni^{2+} is available to fully oxidize the remaining manganese ions in the spinel structure. The unchanged Mn^{4+} ions during the electrochemical reactions improve the stability of the structure by eliminating Jahn-Teller distortion. In 1996, Gao *et al.* found that the lithium in the tetrahedral 8a sites of LNMO sites can be extracted.¹⁴⁸ This process occurs at 4.7 V vs. Li^+/Li and has been reported to involve the oxidation of Ni^{2+} to Ni^{4+} . Since then, LNMO has been extensively studied as one of the most promising high voltage cathode materials.¹⁴⁹

The spinel structure of LNMO is a cubic close packing of oxygen atoms with Mn and Ni occupying half of the octahedral sites and Li residing in an eighth of the tetrahedral sites. LNMO spinels have two types of crystal structure, namely the ordered P4_332 phase and the disordered $\text{Fd}3\text{m}$ phase.^{150, 151} In the P4_332 phase, Ni and Mn are located in an ordered fashion in the octahedral 4b and 12d sites, respectively, with Li ions occupying the 8c sites and O ions in the 8c and the 24e sites. For the $\text{Fd}3\text{m}$ phase, Ni and Mn randomly distribute in the 16d sites, with Li and O ions occupying the 8a and 32e sites, respectively. Previous studies have tried to compare the electrochemical performance of the two phases. However, conflicting results are found in the literatures, which might be caused by the complicated performance influencing factors of LNMO.^{150, 152–154} Besides crystal structure, particle shapes and sizes also play a critical role in determining the performance of the electrode materials. Therefore, the factors which influence the electrochemical performance should be synergistically taken into consideration for the development of advanced spinel cathode. As shown in Fig. 7, we have systematically investigated the combined influence of phase (crystal structure) and particle morphologies (size, shape, and surface area) on LNMO's electrochemical performance. Four

representative LNMO samples with different particle sizes and crystal structures were synthesized: micro-size P₄₃₃₂ (LNMO-MP), micro-size Fd3m (LNMO-MF), nano-size P₄₃₃₂ (LNMO-NP), and nano-size Fd3m (LNMO-NF).¹⁴ LNMO-MP and LNMO-MF had a uniform particle size of about 1 μm , while the particle size of LNMO-NP and LNMO-NF were around 50 nm. A small plateau in the 4.0 V region (assigned to Mn⁴⁺/Mn³⁺ redox couple) was observed in the profiles of LNMO-MF and LNMO-NF, but this was not observed in the profiles of both LNMO-MP and LNMO-NP. The 4.0 V region indicated the existence of Mn³⁺ in the two Fd3m phase samples. Rate capability tests showed that the disordered LNMO spinels exhibited higher rate capability than that of the ordered spinels. This trend was amplified at higher rates. However, the superiority decreased when the size of the LNMO particles is on the nanometer scale. For the ordered phase, the nanosized sample exhibited much better performance than its micro-size counterpart. The rate capability of the four samples could be ranked in the following order, LNMO-MP < LNMO-NP < LNMO-MF \approx LNMO-NF. This result indicated that the disordered structures afford intrinsically better rate capability, and nanosizing is effective in achieving high rate capability. When cycling at 1C for 100 cycles,

the capacity retention of LNMO-MP, LNMO-MF, LNMO-NP, and LNMO-NF were 93.7%, 98.4%, 95.7%, and 92.4%, respectively. The LNMO-MF displayed the highest capacity retention at 1C because of the synergistic effects of micro-size with smaller specific surface area to reduce the contact between the electrolyte and the disordered phase which ensured fast Li diffusion for Li⁺ extraction and insertion. However, at higher rates ($\geq 5\text{C}$), LNMO-NP showed the highest capacity retention. Moreover, the LNMO-NP presented the smallest change of capacity retention. These results suggested that spinel LNMO phase with disordered cation distributions favors high-rate capability, while the presence of an ordered phase benefits cyclability. Meanwhile, forming nanosized spinel particles greatly improved the high rate performance but worsened the cycling performance. The phase- and size-dependent behaviors could be understood in terms of ionic and electronic diffusion, structural variation, and side reactions associated with Mn³⁺. By synergistically considering phase and size effects, we achieved excellent electrode performance with LNMO-MF (micro-sized and disordered phase) and LNMO-NP (nanosized and ordered phase) spinels, delivering the discharge capacities of near 130 mAh·g⁻¹ at 5C and sustaining the capacity retention of exceeding 90% after 300 cycles.

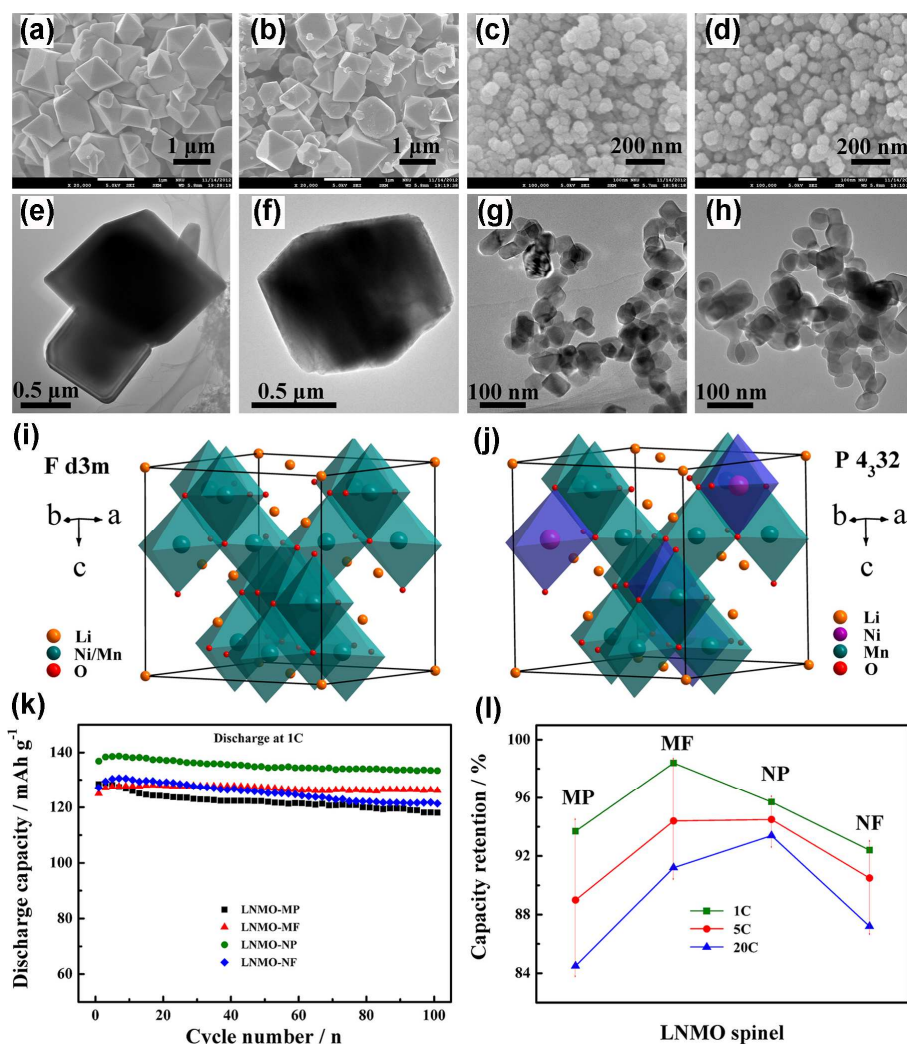


Fig. 7. SEM (a, b, c, d) and TEM (e, f, g, h) images of LNMO-MP (a, e), LNMO-MF (b, f), LNMO-NP (c, g), and LNMO-NF (d, h). Crystal structure of Fd3m phase (i) and P₄₃₃₂ phase (j) LNMO. (k) Cycling performance at 1C and (l) capacity retention at different discharge rates after 100 cycles for LNMO-MP, LNMO-MF, LNMO-NP, and LNMO-NF. Reproduced with permission from ref. 14, Copyright 2013, Springer.

Our previous work has also been focused on constructing 1D nanostructure for spinel LiMn_2O_4 to improve its rate capability and cycle stability. The same strategy has been implied to $\text{LiNi}_{0.5}\text{Mn}_{1.5}\text{O}_4$ too. Two different 1D structures (nanorods and porous nanorods) were constructed and explored.^{66, 155} $\text{LiNi}_{0.5}\text{Mn}_{1.5}\text{O}_4$ nanorods (LNMO-NR) were prepared by an impregnation method followed by a simple solid-state reaction with MnO_2 nanorods as the morphology template. $\text{LiNi}_{0.5}\text{Mn}_{1.5}\text{O}_4$ porous nanorods (LNMO-PNR) were obtained by a morphology inheritance method with porous Mn_2O_3 nanowires/rods. Fig. 8 shows the SEM and TEM images of LNMO-NR and LNMO-PNR. The LNMO-NR showed typical nanorod shape with the diameter around 50 nm and the length of 2–3 μm . Numerous crystal grains with arbitrary stacked arrangement in the nanorods were observed in the TEM images. X-ray diffraction pattern and Raman spectroscopy proved that LNMO-NR adopted

$\text{P4}_3\text{32}$ phase structure. The LNMO-PNR exhibited a 1D wire or rod shape, with the diameter of 100–400 nm and the length of more than 10 μm . TEM image showed that the LNMO-PNR was composed of interconnected nanosized subunits with porous structure. The LNMO-PNR also presented $\text{P4}_3\text{32}$ phase structure. Although we have proved that $\text{P4}_3\text{32}$ phase did not benefit fast Li ion diffusion, this drawback of $\text{P4}_3\text{32}$ phase LNMO could be compensated by the short diffusion distance in the 1D structure. On the other side, $\text{P4}_3\text{32}$ phase structure could benefit the cycling stability of LNMO with 1D structure. LNMO-NR exhibited discharge capacities of 120 and 101 mAh g^{-1} at 20 and 80C, respectively. After 80 cycles at 20C, the capacity retention was 95%. For LNMO-PNR, remarkable capacity retention was achieved in the long-term cycling test (91% capacity retention after 500 cycles at 5C).

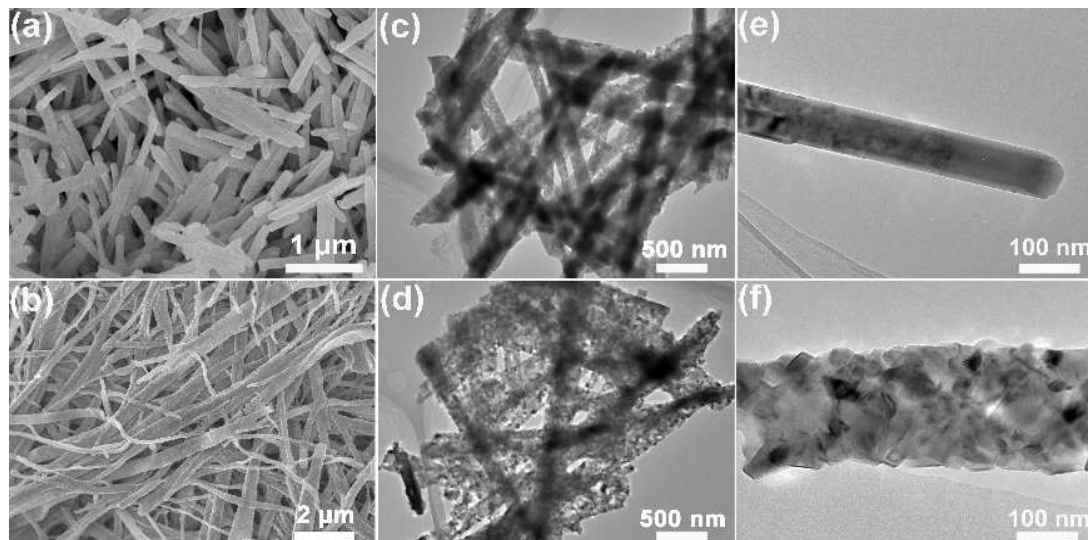


Fig. 8. SEM images of LNMO-NR (a), LNMO-PNR (b) and TEM images of LNMO-NR (c, e) and LNMO-PNR (d, f). Reproduced with permission from refs. 66 and 155, Copyright 2013, American Chemical Society and Copyright 2013, Elsevier B.V.

ARTICLE

Though nanosized LNMO has high gravimetric capacity, its tap density is relatively low compared to commercialized LiCoO₂ (2.6 g cc⁻¹). It is thus that we synthesized hierarchical micro-nano structured LNMO with high tap density of 1.7 g cc⁻¹ via a facile PEG-assisted co-precipitation method.¹⁵⁶ Its discharge capacity at 40C was more than 120 mAh g⁻¹ and the capacity retention at 5C reached 89% after 150 cycles. Lou's group¹⁵⁷ prepared hollow LNMO spheres and cubes via a solid state reaction using porous MnO₂ spheres and cubes as precursors, and the hollow structures delivered discharge capacities of 118 mAh g⁻¹ at 1C and 104 mAh g⁻¹ at 20C.

Besides nanostructures, cation doping is also an effective approach to improve the cycling and rate performance of spinel LNMO.^{158–160} Yang *et al.*¹⁵⁸ used first-principles based on the density functional theory (DFT) to investigate the electronic and structural characteristics of LiM_{0.125}Ni_{0.375}Mn_{1.5}O₄ (M = Cr, Fe, and Co) cathode. The results showed Co-doping would effectively enhance the electronic conductivity and reduce lithium diffusion barrier. Manthiram's group¹⁶⁰ prepared LiNi_{0.5-x}M_xMn_{1.5}O₄ (M = Cr, Fe, and Ga; 0 ≤ x ≤ 0.08) by solid state reaction. These dopant cations aggregated in the surface to form more stable interface, leading to improved cyclability at both room temperature and 55 °C.

Despite the multiple advantages, spinel LNMO shows the drawback of a much lower theoretical capacity than layered metal oxides. Composite cathode materials such as Li₂MnO₃/LNMO and LNMO/layered heterostructured materials are effective in enhancing electrode capacity as well as maintaining partial of LNMO's advantages. On the basis of our previous works, we have synthesized a series of intergrown *x*LiNi_{0.5}Mn_{1.5}O₄·(1-*x*)LiNi_{1/3}Co_{1/3}Mn_{1/3}O₂ (*x*LNMO·(1-*x*)NCM) composite nanorods by a similar simple self-support template method.¹⁶¹ The composite exhibited a 1D rod shape, with the diameter around 100 nm and the length of 1–2 μm (Figs. 9a and 9b). The spinel LNMO and layered NCM nanograins showed remarkable structural compatibility in the nanorods. The XRD patterns of *x*LNMO·(1-*x*)NCM showed an gradual evolution from layered rock salt phase to cubic spinel phase, as *x* increases from 0 to 1. As shown in Fig. 9c, typical galvanostatic profiles of the composite displayed two plateaus: a high voltage plateau above 4.5 V and a low voltage plateau below 4.5 V. The high voltage plateau was attributed to spinel LNMO, and the low voltage plateau was attributed to layered NCM. When *x*=0.5, that was 0.5LNMO·0.5NCM, the composite delivered a high discharge capacity of 200 mAh g⁻¹ and a high energy density of 815 Wh kg⁻¹, which was induced by the effective combination of high capacity from NCM and high working voltage from LNMO. Normally, due to the structural instability and phase transformation to spinel-like phase during deep charge process, the theoretical capacity of layered

materials could not be fully utilized. However, the 0.5LNMO·0.5NCM intergrown composite was able to deliver its theoretical capacity, which indicated the complete deintercalation of Li⁺ in both NCM and LNMO parts. This suggested an interaction between the NCM and LNMO in the composite. A two-phase synergy mechanism in the interfaces of layered-NCM and spinel-LNMO was proposed to explain the improved lithium deintercalation ability of the composite. The intergrown composite structure helped to support the unstable layered structure of NCM upon deep charging, leading to complete deintercalation of the residue Li⁺.

Table 5 summarizes the synthetic method, discharge capacity, cyclability, and rate capability of several nanostructured spinel-type Mn-base oxides. Though nanostructure improves the rate and cycling performance of spinel-type Mn-based oxides, the low theoretical specific capacity limits the further development of spinel-type Mn-based oxides.

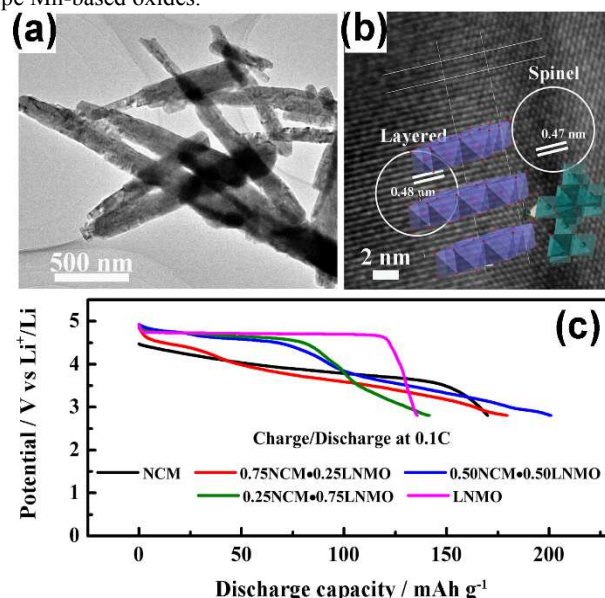


Fig. 9. (a) TEM and (b) HRTEM images with illustrated crystal structure of 0.5LNMO·0.5NCM. (c) Typical discharge curves of *x*LNMO·(1-*x*)NCM composite at a discharge rate of 0.1C. Reproduced with permission from ref. 161, Copyright 2013, The Royal Society of Chemistry.

Table 5. Synthetic method, discharge capacity, cyclability, and rate capability of several nanostructured spinel-type Mn-base oxides as cathode materials of LIBs.

Materials	Synthetic method	Discharge capacity	Capacity retention	Rate capability	Ref.
Porous LiMn ₂ O ₄ nanoparticles	One-pot resorcinol-formaldehyde route	131 mAh g ⁻¹ at 0.5C	84% after 200 cycles at 0.5C	~120 mAh g ⁻¹ at 20C	137
LiMn ₂ O ₄ nanorods	Solid state reaction (β-MnO ₂ nanorods as a	100 mAh g ⁻¹ at 1C	85% after 100 cycles at 1C	-	133

	precursor)				
Porous LiMn₂O₄ nanorods	Solid state reaction (porous Mn ₂ O ₃ nanorods as a precursor)	127 mAh g ⁻¹ at 1C	90% after 500 cycles at 10C	105 mAh g ⁻¹ at 10C	13
LiMn₂O₄ nanowires	Ion-exchange method (Na _{0.44} MnO ₂ nanowires as a precursor)	118 mAh g ⁻¹ at 0.1 A g ⁻¹	92% after 100 cycles at 5 A g ⁻¹	88 mAh g ⁻¹ at 20 A g ⁻¹	138
LiMn₂O₄ nanotubes	Solid state reaction (β-MnO ₂ nanotubes as a precursor)	115 mAh g ⁻¹ at 0.1C	70% after 1500 cycles at 5C	~80 mAh g ⁻¹ at 10C	136
Ordered mesoporous LiMn₂O₄	Solid state reaction (mesoporous MnO ₂ as a precursor)	~100 mAh g ⁻¹ at 0.1C	94% after 500 cycles at 1C	~80 mAh g ⁻¹ at 5C	140
LiMn₂O₄/reduced graphene oxide nanocomposite	Microwave-assisted hydrothermal method	137 mAh g ⁻¹ at 1C	96% after 100 cycles at 10C	101 mAh g ⁻¹ at 100C	142
LiNi_{0.5}Mn_{1.5}O₄ nanoparticles	One-pot resorcinol-formaldehyde synthesis	135 mAh g ⁻¹ at 0.2C	94% after 200 cycles at 1C	118 mAh g ⁻¹ at 20C	153
LiNi_{0.5}Mn_{1.5}O₄ nanorods	Solid state reaction (β-MnO ₂ nanorods as a precursor)	135 mAh g ⁻¹ at 1C	90% after 80 cycles at 20C	120 mAh g ⁻¹ at 20C	155
Porous LiNi_{0.5}Mn_{1.5}O₄ nanorods	Solid state reaction (porous Mn ₂ O ₃ nanorods as a precursor)	140 mAh g ⁻¹ at 1C	91% after 500 cycles at 5C	109 mAh g ⁻¹ at 20C	66
LiNi_{0.5}Mn_{1.5}O₄ hollow spheres	Solid state reaction (porous MnO ₂ hollow structures as precursors)	118 mAh g ⁻¹ at 1C	97% after 200 cycles at 2C	104 mAh g ⁻¹ at 20C	157
LiNi_{0.5}Mn_{1.5}O₄ micro-nano structure	PEG-assisted co-precipitation method	140 mAh g ⁻¹ at 1C	89% after 150 cycles at 5C	120 mAh g ⁻¹ at 40C	156
Carbon-coated LiMn₂O₄ clusters	Hydrothermal method combined with sucrose carbonization	120 mAh g ⁻¹ at 1C	63% after 2000 cycles at 20C	56 mAh g ⁻¹ at 300C	143
0.5LiNi_{0.5}Mn_{1.5}O₄·0.5LiNi_{1/3}Co_{1/3}Mn_{1/3}O₂ nanorods	Template method	200 mAh g ⁻¹ at 0.1C	87% after 100 cycles at 0.2C	~110 mAh g ⁻¹ at 2C	161

3.4 Polyanion-type Mn-based oxides

Polyanion-type Mn-based oxides mainly include olivine-type LiMnPO₄ and silicate-type Li₂MnSiO₄. Polyanion-type Mn-based oxides possess higher thermal stability than layered Mn-based oxides owing to the stronger covalent bonds of oxygen atoms, leading to better safety. Moreover, polyanion-type Mn-based oxides have higher theoretical specific capacities than those of spinel-type Mn-based oxides, resulting in their higher energy density. However, polyanion-type Mn-based oxides are plagued by poor electronic transport and ionic diffusion. Nanostructures are attempted to solve this problem.

3.4.1 Olivine-type LiMnPO₄

The olivine-type LiMnPO₄ is reported by Goodenough's group in 1997.¹⁶² LiMnPO₄ possesses an olivine structure with Pnma symmetry, in which oxygen lattice has a hexagonal close-packed (hcp), Li and Mn metal atoms occupy half of the octahedral sites, and P atoms occupy 1/8 of the tetrahedral sites (Fig. 10a).¹⁶³ Li⁺ ions diffuse along the 1D [010] direction (*i.e.*, a-axis), so (010) plane and [010] direction are very important for its electrochemical performance. LiMnPO₄ has a high operating voltage of 4.1 V vs. Li⁺/Li with a theoretical specific capacity of 170 mAh g⁻¹ based on Mn³⁺/Mn²⁺ redox couple. However, it suffers from very low intrinsic electronic conductivity (less than 10⁻¹⁰ S cm⁻¹) and the large structure distortions induced by Jahn-Teller effect of Mn³⁺ ions, leading to low practical capacity and poor rate performance.¹⁶⁴ Preparing nanostructured LiMnPO₄ combined with carbon coating and cation doping is an effective route to solve these problems.¹⁶⁵⁻¹⁶⁹ Cho's group¹⁶⁵ synthesized 3D macroporous LiMnPO₄/C flakes

which consisted of many nanoparticles with particle size of ~6 nm embedded in a carbon matrix. The flakes delivered discharge capacities of 162 mAh g⁻¹ at 0.1C and 110 mAh g⁻¹ at 10C. Dominko's group¹⁶⁷ designed a two-step sol-gel route to prepare LiMnPO₄/C nanocomposite. The composite showed a capacity of 165 mAh g⁻¹ at 55 °C with a capacity decay of 0.1% per cycle over 240 cycles. Crystallographic orientation is also very important for LiMnPO₄ because of its 1D Li⁺ ion diffusion path.^{76, 164, 170} Choi *et al.*⁷⁶ fabricated porous LiMnPO₄/C nanoplates via a solid-state reaction. The porous nanoplates with a thickness of ~50 nm were assembled by nanorods growing along the [010] direction in the (100) plane. The specific capacity reached 168 mAh g⁻¹ at 0.02C. Furthermore, doping LiMnPO₄ with Fe is a common way to enhance conductivity and stability.^{169, 171-174} Aurbach's group¹⁷¹ prepared LiMn_{0.8}Fe_{0.2}PO₄/C nanocomposite by a solid state reaction and the composite exhibited a capacity of ~165 mAh g⁻¹ at 0.1C. Cui's and Dai's groups¹⁷² used solvothermal method to manufacture LiMn_{0.75}Fe_{0.25}PO₄ nanorods/rGO hybrid material. The composite delivered capacities of 155 mAh g⁻¹ at 0.5C and 132 mAh g⁻¹ at 20C, respectively. Scrosati's and Sun's groups¹⁶⁹ designed double-structured LiMn_{0.85}Fe_{0.15}PO₄ modified with LiFePO₄. The LiMn_{0.85}Fe_{0.15}PO₄-LiFePO₄/C composite displayed a high volumetric energy density of 970 Wh m⁻³.

3.4.2 Li₂MnSiO₄

Li₂MnSiO₄ is attractive mainly for the possible 2e⁻ exchange reaction based on Mn³⁺/Mn²⁺ and Mn⁴⁺/Mn³⁺ redox couples, giving a theoretical capacity of 333 mAh g⁻¹.¹⁶³ As shown in Fig. 10b, Li₂MnSiO₄ possesses four kinds of crystal structures including Pmn₂, Pmnb, P2₁/n, and Pn symmetry.¹⁷⁵ Like LiMnPO₄,

$\text{Li}_2\text{MnSiO}_4$ similarly is also plagued by low intrinsic electronic conductivity (less than $10^{-14} \text{ S cm}^{-1}$) and the Jahn-Teller distortions of Mn^{3+} ions. Furthermore, $\text{Li}_2\text{MnSiO}_4$ undergoes the gradual reduction of crystallinity during the cycling derived from the Li–Mn position exchange. Common strategies to solve the problems include designing the nanostructures, doping with other cations, and coating with carbon.^{20, 176–180} Carbon coating can obviously enhance the electronic conductivity and partially impact on the Li^+ ion diffusion coefficient. Decreasing the particle sizes can shorten the diffusion path for Li^+ ions. Cation-doping can modify the intrinsic properties of $\text{Li}_2\text{MnSiO}_4$ such as conductivity and structural stability. Yang's group¹⁷⁶ prepared $\text{Li}_2\text{MnSiO}_4/\text{C}$ nanocomposite with a capacity of 209 mA h g^{-1} at 5 mA g^{-1} , which achieves more than one electron reaction in silicate cathode materials for the first time. Kuezman *et al.*¹⁷⁷ synthesized $\text{Li}_2\text{MnSiO}_4/\text{C}$ nanoparticles with a particle size of 15–100 nm by a microwave assisted solvothermal method, and the nanoparticles showed a discharge capacity of 250 mA h g^{-1} at 50°C and 0.1 C. Our group²⁰ fabricated $\text{Li}_2\text{MnSiO}_4@\text{C}$ nanocomposite with low carbon content of 5 wt.% via a hydrothermal-assisted

solution route and the composite exhibited an initial discharge capacities of $281.5 \text{ mA h g}^{-1}$ at 25°C and $321.4 \text{ mA h g}^{-1}$ at 45°C . Manthiram's group¹⁷⁸ used template method to prepare $\text{Li}_2\text{MnSiO}_4/\text{C}$ nanocomposite with hierarchical macro/mesoporosity which delivered a reversible discharge capacity of 200 mA h g^{-1} at 0.1C.

Table 6 summarizes the synthetic method, discharge capacity, cyclability, and rate capability of several nanostructured polyanion-type Mn-base oxides. It is pointed out that polyanion-type Mn-base oxides are hampered by sluggish kinetics, so carbon-coating with nanostructure is widely used. However, their cycling and rate performance is still difficult to meet the commercial requirements. Which kind of materials would really fulfill future applications such as electric vehicles, Li-rich layered Mn-base oxides, spinel Mn-base oxides or polyanion-type Mn-base oxides? There is no clear answer up to now, and further investigation is needed. Designing the combination to form composites or developing new cathode materials should be a recommendable option.

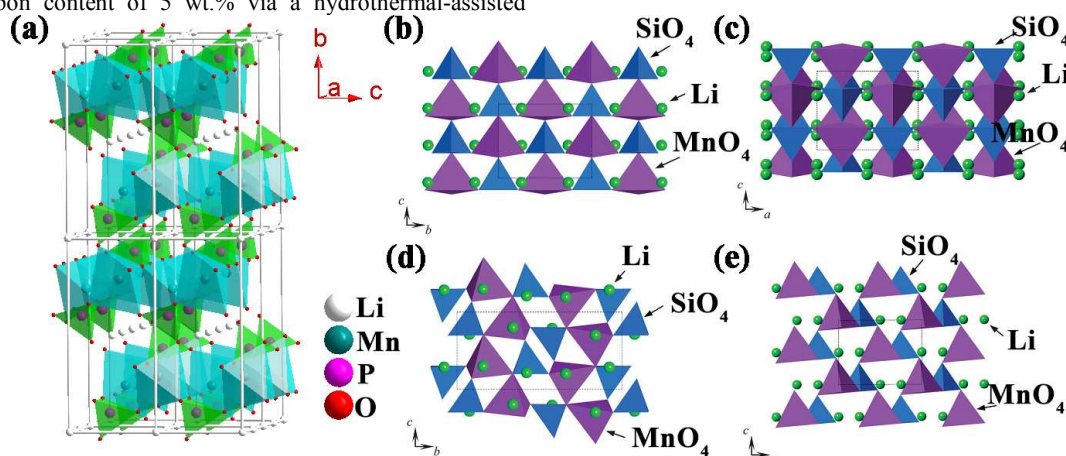


Fig. 10. (a) Crystal structure for LiMnPO_4 viewed along the b-axis which is composed of pairs of PO_4 tetrahedral (orange) and MnO_6 octahedral (green). Four kinds of $\text{Li}_2\text{MnSiO}_4$ crystal structures composed of MnO_4 (purple) and SiO_4 (blue) tetrahedral together with Li ions (green): (b) orthorhombic $\text{Pmn}2_1$ phase; (c) orthorhombic Pmnb phase; (d) monoclinic $\text{P}2_1/n$ phase; (e) monoclinic Pn phase. Reproduced with permission from refs. 175, Copyright 2013, The Royal Society of Chemistry.

Table 6. Synthetic method, discharge capacity, cyclability, and rate capability of several nanostructured polyanion-type Mn-base oxides as cathode materials of LIBs.

Materials	Synthetic method	Carbon content	Discharge capacity	Capacity retention	Rate capability	Ref.
3D macroporous LiMnPO_4/C flakes	Template method	11 wt.%	162 mA h g^{-1} at 0.1C	98% after 40 cycles at 1C	110 mA h g^{-1} at 10C	165
LiMnPO_4/C nanocomposite	Ball milling	30 wt.%	158 mA h g^{-1} at 0.05C	88% after 50 cycles at 0.5C	107 mA h g^{-1} at 2C	166
LiMnPO_4/C nanocomposite	Two-step sol-gel route	14 wt.%	165 mA h g^{-1} at 0.05C	~73% after 240 cycles at 0.05C	~80 mA h g^{-1} at 2C	167
LiMnPO_4/C nanoplates	Solid state Reaction	20 wt.%	168 mA h g^{-1} at 0.04C	95% after 50 cycles at 0.04C	117 mA h g^{-1} at 1C	76
$\text{LiMn}_{0.8}\text{Fe}_{0.2}\text{PO}_4/\text{C}$ nanocomposite	Solid state Reaction	10 wt.%	165 mA h g^{-1} at 0.1C	-	~90 mA h g^{-1} at 10C	171
$\text{LiMn}_{0.75}\text{Fe}_{0.25}\text{PO}_4$ nanorods/rGO composite	Solvothermal method	26 wt.%	155 mA h g^{-1} at 0.5C	-	107 mA h g^{-1} at 50C	172
Double-structured $\text{LiMn}_{0.85}\text{Fe}_{0.15}\text{PO}_4$ modified with LiFePO_4/C	Co-precipitation method	2.9 wt.%	~155 mA h g^{-1} at 0.1C	97% after 50 cycles at 1C	~90 mA h g^{-1} at 5C	169
$\text{Li}_2\text{MnSiO}_4/\text{C}$ nanoparticles	Microwave assisted solvothermal method	31.7 wt.%	250 mA h g^{-1} at 0.1C	-	-	177
$\text{Li}_2\text{MnSiO}_4/\text{C}$ nanoparticles	Hydrothermal-assisted solution route	5 wt.%	282 mA h g^{-1} at 0.05C	69% after 40 cycles at 0.15C	141 mA h g^{-1} at 3C	20

Li₂MnSiO₄/C nanocomposite with hierarchical macro/mesoporosity	Template method	20 wt.%	225 mAh g ⁻¹ at 0.1C	52% after 50 cycles at 1C	170 mAh g ⁻¹ at 1C	178
---------------------------------------------------------------------------------------------	-----------------	---------	---------------------------------	---------------------------	-------------------------------	-----

4. Mn-based oxides as oxygen electrocatalysts for metal–air batteries

Oxygen electrocatalysts play a crucial role in determining the power density, cycling capability, and energy conversion efficiency of metal–air batteries and fuel cells.^{4, 181–185} Oxygen reduction reaction (ORR) occurs in the cathode of metal–air batteries and fuel cells, which plays a key role to the electrochemical performance. Table 7 summarizes the several reaction processes of ORR which mainly include 4e or 2e pathway. Extensive efforts have focused on searching efficient ORR catalysts for many years.^{186–191} At present, Pt and Pt alloys are known to be the best active catalysts for ORR, but they have lost their brilliance owing to the high price and unsatisfied stability. Therefore, it is extremely essential for us to develop alternative catalysts based on non-noble elements. Among them, Mn-based oxides are particularly attractive due to their high abundance, low cost, environment friendliness and considerable electrocatalytic activity.^{15, 21, 22, 189, 192–195} In addition, the variable state (*e.g.*, +2, +3, +4, +6, and +7) and coordination structures (*e.g.*, MO₆ octahedral and MnO₄ tetrahedron) of Mn (Fig. 11) lead to rich redox electrochemistry and material chemistry, offering opportunities and challenges for searching and developing non precious metal based catalysts.^{15, 21, 22, 189}

Table 7. Several kinds of reaction processes of oxygen reduction reaction (ORR).

Reaction condition	Reaction process	Potential (V vs. SHE)
Alkaline aqueous solution	$O_2 + H_2O + 4e^- \rightarrow 4OH^-$	0.401
	$O_2 + H_2O + 2e^- \rightarrow HO_2^- + OH^-$	-0.065
	$HO_2^- + H_2O + 2e^- \rightarrow 3OH^-$	0.897
Acidic aqueous solution	$O_2 + 4H^+ + 4e^- \rightarrow 2H_2O$	1.229
	$O_2 + 2H^+ + 2e^- \rightarrow H_2O_2$	0.700
	$H_2O_2 + 2H^+ + 2e^- \rightarrow 2H_2O$	1.760
Aprotic solvent	$O_2 + 2e^- \rightarrow O_2^{2-}$	

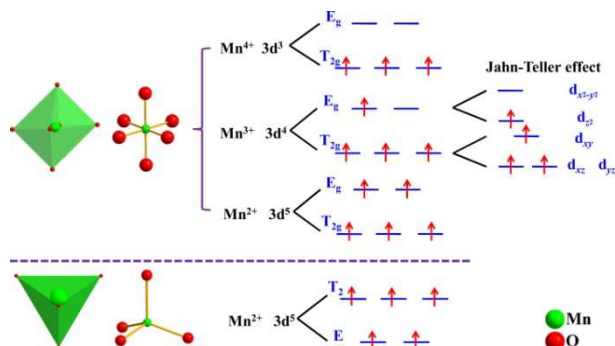


Fig. 11. Coordination structure and valence state of Mn cations in Mn-based oxides.

4.1 Binary Mn-based oxides

Mn-based oxides can simultaneously serve as electrocatalysts for oxygen reduction and evolution, rendering their bifunctional role for oxygen electrochemistry. Since MnO₂ was first reported for the ORR

in early 1970s,¹⁹⁶ many studies have been devoted to studying and optimizing MnO_x-based catalysts for air electrodes.^{22, 189, 192–195} Possible motivation is the μ-oxido-CaMn₄O_x cluster catalytic active centre to oxidize water in photosystem II in nature.^{197–199} Electrochemically active Mn-based oxides such as Mn₅O₈, Mn₃O₄, Mn₂O₃, MnO₂, and MnOOH all exhibit considerable ORR activities in alkaline media.^{46, 193, 194, 200, 201} The composition, crystalline structure, morphology, oxidation state, and surface area can affect the electrocatalytic properties. For example, the catalytic activities depend strongly on the crystallographic structure, decreasing in the order of α- > β- > γ-MnO₂ for 1D MnO₂ nanostructure.⁴⁶ The change is ascribed to the combinative effect of their intrinsic tunnel (built up with MnO₆ octahedron) size and electronical conductivity. Ohsaka's group²⁰² reported that the catalytic activities are decreased in the order of MnOOH > Mn₂O₃ > Mn₃O₄ > Mn₅O₈ owing to the influence of the valence and coordination environment of Mn. Meanwhile, among the same phase, α-MnO₂ nanospheres and nanowires apparently outperform the benchmark micro-sized particles because of smaller size and higher specific surface area. Moreover, the nature of preferentially exposed facets could also influence the catalytic activity of binary Mn-based oxides, which requires further identification.²⁰¹

Additionally, it seems to be an efficient strategy to enhance the ORR activity by doping another component. MnO_x combined with a variety of elements (*e.g.*, Pt, Pd, Ni, Mg, Ca) exhibits superior activity than both pristine metals and non-doped materials.^{46, 193, 203, 204} The results from Roche *et al.*¹⁹⁴ demonstrated that the doped Ni-MnO_x/C and Mg-MnO_x/C nanoparticles promoted the ORR toward direct 4e pathway: first quasiaequilibrium proton insertion process to form intermediate MnOOH, the second O₂ adsorption onto surface sites upon MnOOH, the third rate-determining electron transfer step consisting of electrospitting of adsorbed O₂ species to O_{ads} state, and finally the electrochemical reduction of O_{ads} to hydroxide anions. The Mn^{III}/Mn^{IV} redox couple acts as the oxygen acceptor and donor mediator, thus favoring the electron transfer. Other examples such as manganese oxide nanoparticles electrodeposited on Pt substrate¹⁹³ or Pd nanoparticles supported on MnO₂²⁰⁴ nanorods all exhibit superior catalytic activity to pristine noble metals and single manganese oxides. Consequently, the ORR performance is improved by the doped MnO_x electrocatalysts.

Other strategies have also been designed to enhance the electrocatalytic performance of binary Mn-based oxides including optimizing morphologies, coating with metals or integrating conductive nanostructures.^{46, 193, 194, 203, 204} Although these methods have been proved to be effective, they are relatively complex and expensive. Recently, a facile and economic route has been developed to improve the electrocatalytic activity of rutile-type β-MnO₂ nanorods by introducing native oxygen defects without modification by foreign additives (Fig. 12a).¹⁹² As shown in Fig. 12b, heat treatment in argon and air leads to different concentration of oxygen nonstoichiometry, accompanied with the reduction of Mn⁴⁺ to Mn³⁺, while still maintains pristine 1D nanostructure morphology. More interestingly, two domains can be observed in oxygen-vacancy samples after heat treatment (Fig. 12d), which is indicative of a typical pyrolusite lattice and a new structure. The different fast Fourier transformation profile and new lattice fringes can be attributed to reconstruction and phase transformation, which correspond to oxygen-defect-induced structural variation of MnO₂. Electrochemical results demonstrate that modest concentration of oxygen-defective oxide exhibits more positive potential, larger reduction current and lower peroxide yield of the ORR

electrocatalysis and the enhanced oxygen evolution reaction (OER) catalysis. DFT computational investigations reveal that the improved performance is contributed to modified MnO_2 surface-oxygen interaction and a reduced kinetic barrier with the presence of oxygen vacancies (Fig. 12e).

Recently, many efforts focus on developing metal–air primary batteries such as Mg–air, Al–air, and Zn–air batteries.^{50, 205, 206} Cheap Mn-based oxides have shown high ORR catalytic performance, while the reports on Mn-based oxides as the cathode catalysts of metal–air primary batteries are relative few. Ni modified MnO_x/C delivered a power density of 122 mW cm^{-2} in the Zn–air primary batteries, which is comparable to the Pd/C and Pt/C catalysts.²⁰⁷ Besides catalysts, there are still many problems which hinder the wide application of zinc–air batteries. First, the electrolyte is very easy to leakage. Second, the solution is evaporated to dry the electrolyte. Third, the electrolyte is moisture absorbent to decrease the pH value. Last, CO_2 in the air can react with alkaline electrolyte. If the above problems are solved, Mn-based oxides would be more useful.

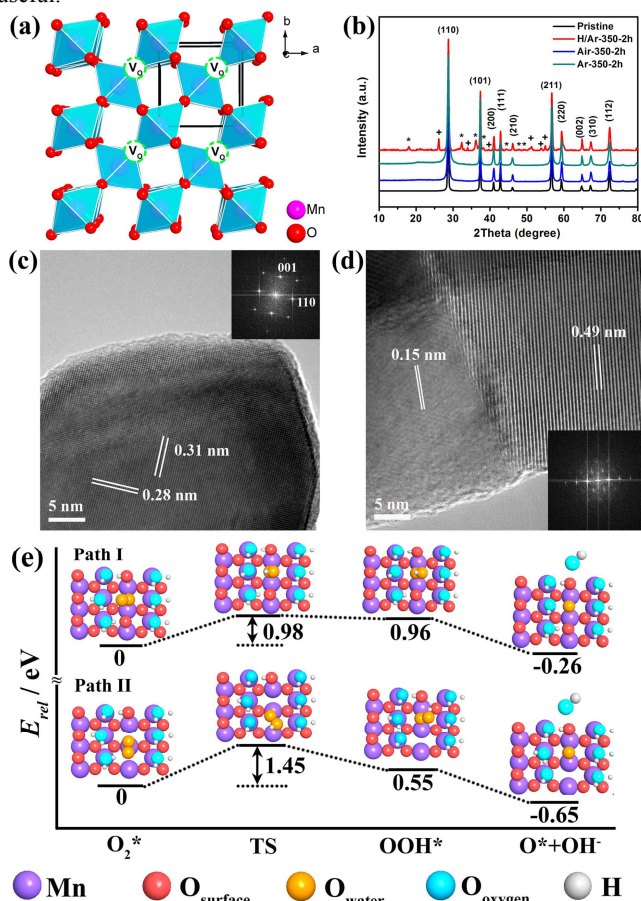


Fig. 12. (a) Structure of rutile-type MnO_2 with oxygen vacancies. (b) XRD patterns of different oxides. The symbols * and + denote Mn_3O_4 and MnOOH , respectively. HRTEM images of pristine $\beta\text{-MnO}_2$ (c) and $\beta\text{-MnO}_2$ heated in Ar (d), the insets show the FFT patterns. (e) Energy profiles and configurations of ORR on $\beta\text{-MnO}_2$ surfaces with one (Path I) and two (Path II) oxygen vacancies. Asterisks denote adsorbed species. TS=transition state. Reproduced with permission from ref. 192, Copyright 2013, Wiley-VCH.

In addition to aqueous systems, binary manganese oxides have also been applied as oxygen electrocatalysts in nonaqueous systems.^{195, 208–210} For instance, Li– O_2 batteries based on $\alpha\text{-MnO}_2$

nanowires showed a capacity of 3000 mAh g^{-1} (based on carbon) and excellent capacity retention after 10 cycles.¹⁹⁵ Furthermore, MnO_2 nanowire exhibits much higher capacity than bulk MnO_2 among both α - and $\beta\text{-MnO}_2$ phase, suggesting that the morphology and structure of MnO_x play an important role in determining the catalytic activity in organic electrolyte, which is similar to that in aqueous electrolyte. Other investigation demonstrates that the single-crystalline $\alpha\text{-MnO}_2$ nanotubes display much better lithium–air batteries performance than $\alpha\text{-MnO}_2$ nanowires and $\delta\text{-MnO}_2$ nanosheets because the former possesses higher surface area to the surrounding electrolyte and faster electrons and Li^+ ions transport.²¹¹ Recently, a virus biotemplated method has been developed to synthesize $\delta\text{-MnO}_2$ nanowires for Li– O_2 battery application, and the nanowires shows improved performance than its counterpart nanoparticle.²¹² Our group⁴¹ synthesized sponge-like 3D nanostructured $\varepsilon\text{-MnO}_2/\text{Ni}$ foam nanocomposite by electrodeposition. The composite showed a high discharge capacity of 6300 mAh g^{-1} at 500 mA g^{-1} with superior cyclability of 120 cycles at 2.2–4.3 V. As to the cathode catalysts in Li–air batteries, many factors including oxidation state of manganese, crystallite size, surface area and pore volume are all found to have greatly effects on the catalytic performance.^{211, 213}

4.2 Mn-based composite oxides

Mn-based composite oxides adopting spinel or perovskite structure have been largely studied as ORR and OER catalysts and their application in rechargeable metal–air batteries are discussed in this section.^{15, 21, 22, 189} Extra advantages of composite oxides commonly include improved structural durability and the combination effect of several types of electrochemical active sites. These active sites are favorable to promote the ORR and OER, making them possible as bifunctional catalysts for air cathode in rechargeable metal–air batteries.^{4, 184}

4.2.1 Spinel-type Mn-based oxides

Spinel is a class of oxides with the formula AB_2O_4 , where generally A represents a divalent metal ion (e.g., Mg, Mn, Fe, Co, Ni or Zn) and B stands for a trivalent metal ion (e.g., Al, Fe, Co, Cr or Mn). Among various spinels, MMn_2O_4 is particularly attractive owing to the natural advantages of manganese element such as high nature abundance, low price, and environmental friendliness. Since Mn-based spinels possess electronic conductivity or semiconductivity and $\text{Mn}^{4+}/\text{Mn}^{3+}$ redox couple, their physicochemical performance is closely related to the composition, crystalline structure, surface area, and oxidation state of metal ions, which are greatly determined by synthetic conditions.²¹⁴ Traditionally, these spinel compounds have been prepared by high-temperature solid-solid reaction using the mixing of stoichiometric amounts of appropriate metal oxides, and the heat treatment temperature is often over $1000 \text{ }^\circ\text{C}$ for several hours, or even periods of few days.²¹⁵ The materials synthesized by this method are difficult to control the particle size and shape, thus displaying limited electrochemical activity. Recently, a facile and rapid room-temperature methodology has been developed for achieving highly active spinel nanoparticles.²¹ The formation is accomplished by reduction-recrystallization of amorphous MnO_2 precursors in aqueous solution containing divalent metal ions such as Co^{2+} . Two different crystal structures (tetragonal and cubic $\text{Co}_x\text{Mn}_{3-x}\text{O}_4$ spinels) were obtained using NaH_2PO_2 (CoMnO-P) and NaBH_4 (CoMnO-B) as the reducing agents, respectively. The as-prepared Co–Mn–O nanocrystalline spinels inherited the morphology of the amorphous nanoparticle MnO_2 precursor and performed remarkably higher activity towards dual ORR/OER due to high surface area, large

concentration of lattice defects, and abundant vacancies compared to the counterparts synthesized at high temperature. Interestingly, the cubic Co-Mn-O spinel outperformed the tetragonal phase in catalyzing the ORR (Fig. 13a), while the tetragonal spinel surpassed the cubic phase for the OER (Fig. 13b). This phase-dependent electrocatalytic character was contributed to the different binding energies of oxygen adsorption on the surface of the two phases, which were revealed by both experimental and computational analysis (Figs. 13c and 13d). Furthermore, the active Co-Mn-O spinel was applied as an air electrode to fabricate coin-type Zn-air cells, which exhibited stable galvanostatic discharge profile and remarkable specific energy densities. Following the similar synthetic procedure, nanospheres and nanocubes of $ZnMn_2O_4$ spinels have also been successfully prepared and shown considerable electrocatalytic performance.²¹⁶ These illustrated examples provide the feasibility of reasonable design and controllable synthesis of nanostructured composite spinel oxides as bifunctional electrocatalysts for air electrodes which can serve rechargeable metal-air batteries and fuel cells.

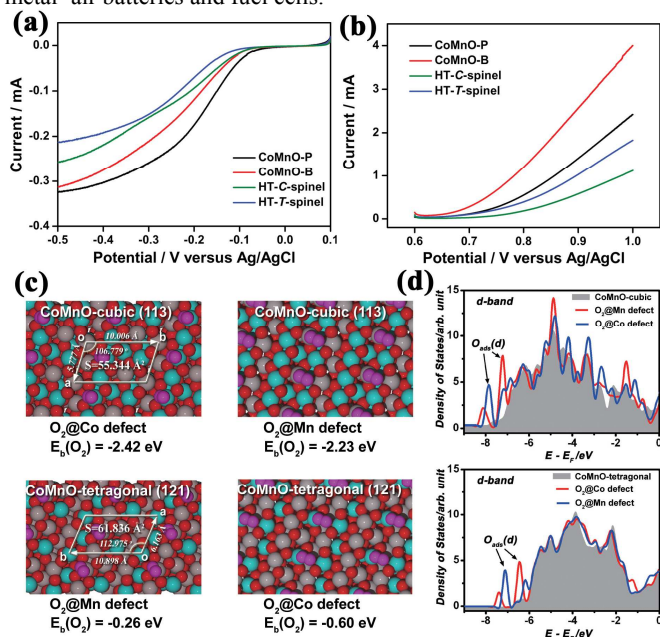


Fig. 13. Voltammograms of the (a) ORR and (b) OER recorded on different catalysts. Comparisons are also given to the counterpart cubic-phase (HT-C-spinel) and tetragonal-phase (HT-T-spinel) bulk spinels synthesized using a high-temperature ceramic method. First-principle study of surface oxygen adsorption on different sites of cubic and tetragonal spinel phases. (c) Geometries and binding energies of oxygen molecules (purple) on cobalt (cyan) or manganese (grey) defect sites. (d) Corresponding density of states of bare and O₂-adsorbed spinels. Red spheres represent lattice oxygen. Reproduced with permission from ref. 21, Copyright 2011, Nature Publishing Group.

Besides standard spinel structure, post-spinel 1D $CaMn_2O_4$ nanorods prepared by solvothermal route at mild temperature has been reported.²¹⁷ The reaction parameters including solvent, heating temperature, and dwell time are all found to affect the phase formation of $CaMn_2O_4$. The as-prepared $CaMn_2O_4$ nanorods were detailedly investigated as electrocatalysts for ORR in alkaline electrolytes and exhibited remarkable catalytic performance with similar mass activities to Pt/C despite of its slightly lower activity. In addition to the considerable catalytic activity, the $CaMn_2O_4/C$ electrocatalyst also afforded better catalytic stability due to the chemical and structural robustness of marokite in an alkaline

environment. $CaMn_2O_4$ nanorods with low cost and high abundance can serve as attractive non-precious ORR catalysts which are widely applied in metal-air batteries and alkaline fuel cells.

Spinel manganese oxides have also been widely used as cathode catalysts for metal-air (mainly Li-air) batteries. For example, multiporous $MnCo_2O_4$ spinel microspheres have been successfully employed as air cathode for Li-O₂ batteries. The assembled cells display low overpotential, high capacity and good cycle performance due to the porous nanostructure of $MnCo_2O_4$ microspheres, which offers high active sites and enough transmission paths for O₂ and Li⁺ ions.²¹⁸ Dai's group^{189, 219} developed a spinel manganese-cobalt oxide/N-doped graphene composite and employed as highly efficient ORR and OER bifunctional electrocatalysis in alkaline solution. When transformed the catalyst to aprotic electrolyte for Li-O₂ batteries, the hybrid based electrode exhibits low overpotential of 0.8 V and enhanced cyclability of 40 cycles at 400 mA g⁻¹ with cutoff capacity of 1000 mAh g⁻¹, which are attributed to the high active spinel nanoparticles and the electrochemical covalent coupling between the oxide and the conducting graphene substrate.²¹⁹

4.2.2 Perovskite-type Mn-based oxides

Perovskite-type oxides with the general formula ABO₃ have a wide range of physical-chemical properties, whereas A is the rare-earth or alkaline-earth metal and B is a transition metal. The perovskite structures allow partial A and B cations substitution to form A_{1-x}A_xB_{1-y}B_yO₃, making researchers tailor their catalytic performance. In general, A-site substitution mainly influences the ability of oxygen adsorption, however, B-site substitution affects the activity of the adsorbed oxygen.¹⁸⁴ Various perovskite oxides with different replacements have been studied for oxygen electrocatalysis. Since Bruce firstly applied La_{1-x}Sr_xMnO₃ in aprotic Li-O₂ batteries, the perovskite-type catalysts have been widely used as cathode catalysts, showing remarkable electrocatalytic performance.²²⁰⁻²²³ Recently, porous La_{0.75}Sr_{0.25}MnO₃ nanotubes were prepared using the electrospinning technique following by a heating procedure.²²² With the novel material as electrocatalyst, Li-O₂ batteries exhibited much lower charge voltage than that of KB and could maintain 124 cycles by controlling the discharging depth of 1000 mAh g⁻¹. The intrinsically high catalytic activities promoted dual ORR/OER, and porous tubular nanostructure provided more void and active sites for the formation and decomposition of the discharge products, thus benefiting the reversibility of the air electrode.

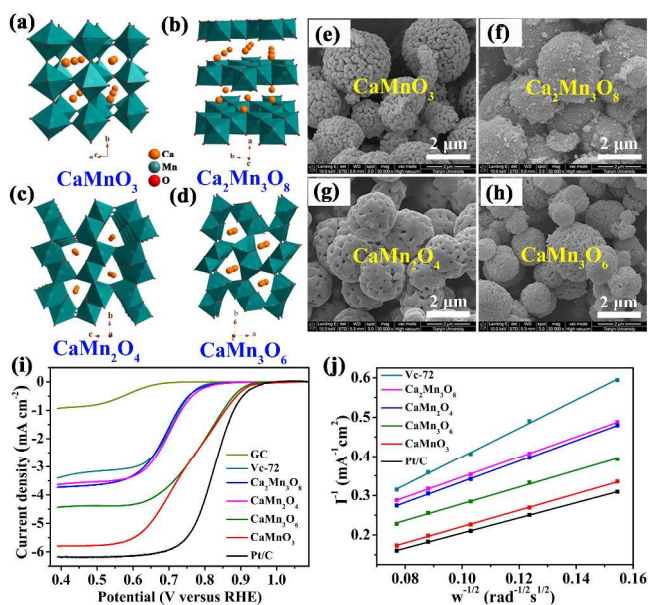


Fig. 14. Schematic crystal structures (a–d) and morphologies (e–h) of CaMnO_3 (a, e), $\text{Ca}_2\text{Mn}_3\text{O}_8$ (b, f), CaMn_2O_4 (c, g), and CaMn_3O_6 (d, h). (i) Linear sweeping voltammograms of CaMnO_3 , $\text{Ca}_2\text{Mn}_3\text{O}_8$, CaMn_2O_4 , CaMn_3O_6 , GC, Vulcan carbon XC-72 and Pt/C recorded at 1600 rpm in O_2 -saturated 0.1 M KOH solution. (j) K–L plots of different catalysts at 0.5 V. Reproduced with permission from ref. 15, Copyright 2012, The Royal Society of Chemistry.

Aiming at searching new ORR catalysts, a series of micro-nanostructured calcium-manganese oxides (Ca-Mn-O) composed of inexpensive and high abundant elements were developed as electrocatalysts for oxygen electrocatalysis (Fig. 14).¹⁵ These porous Ca-Mn-O compounds were synthesized through thermal decomposition of $\text{Ca}_{1-x}\text{Mn}_x\text{CO}_3$ solid solution precursors. The catalytic performance of Ca-Mn-O microspheres greatly depended on the surface oxidation state of Mn and the crystallographic structures, which influenced the extent of O_2 activation. Among the series of Ca-Mn-Os (perovskite-type CaMnO_3 , layered structured $\text{Ca}_2\text{Mn}_3\text{O}_8$, post-spinel CaMn_2O_4 and CaMn_3O_6), the perovskite CaMnO_3 with open MnO_6 tunnels and mixed manganese valence exhibited the highest activities in alkaline electrolyte, including larger current density and higher electron transfer number (Figs. 14i and 14j) with superior catalytic stability compared to the benchmark Pt/C. Following the above results, we synthesized interconnected porous CaMnO_3 nanostructures and investigated their catalytic performance as cathode catalysts for rechargeable Li– O_2 batteries.²²⁴ The CaMnO_3 -based cathode enables much enhanced cyclability (> 80 cycles) with stable discharge terrace than pure carbon based cathode (< 25 cycles) and much lower discharge-charge voltage gap of 0.98 V (*ca.* 620 mV smaller than that of carbon only electrode). The improved performance is attributed to the intrinsic high electrocatalytic activity of CaMnO_3 and the designed porous nanostructure. Supporting a small amount of Pt nanoparticles on porous CaMnO_3 matrix to construct the Pt/ CaMnO_3 nanocomposite can greatly promote the total electrocatalytic performance.²³ The hydrogenated Pt/ CaMnO_3 nanocomposites composed of Pt clusters with particle size of 1 nm and porous cobweb-like CaMnO_3 exhibited an 11-fold higher specific activity than that of the commercial Pt/C catalyst. The remarkable electrocatalytic performance could be attributed to the homogenous dispersion and ultrasmall Pt nanoparticles, the introduced oxygen defects and a multiple valence of Mn (+3 and +4) and the synergistic effect of Pt and CaMnO_3 , which alters the electronic structure of Pt and

facilitates the adsorption/desorption behaviour of oxygen species. Furthermore, the hybrid catalyst shows superior catalytic durability due to the intrinsic chemical stability of CaMnO_3 support and the confinement effect in interconnected nanoporous CaMnO_3 substrate.

Predicting a catalyst design principle which correlates the material properties to the catalytic performance can promote the search for highly active and low-cost transition-metal oxide catalysts. Recent studies have demonstrated that the ORR activity of perovskite family catalysts are primarily related to σ^* -orbital (e_g) occupation (e_g -filling with a value around 1 for maximum activity) and secondarily to the extent of B-site transition metal-oxygen covalent bond (Fig. 15).²² A single e_g electron can provide a moderate strength when breaking the B–OH bond and forming B– O_2^{2-} , thereby, stabilizing the displacement in rate-limiting process. Based on the mechanism analysis, the nature ORR activity of perovskite family displays a volcano shape as function of B ions e_g -filling. Notably, by applying this principle, $\text{LaMnO}_{3+\delta}$ and LaNiO_3 oxides show remarkable intrinsic ORR activity compared to state-of-the-art Pt/C catalyst in alkaline media.²² This principle would provide important guideline for developing highly active non-precious-metal composite oxide catalysts in electrochemical conversion and storage devices.

Recently, perovskite-type compounds as light-harvesting materials have also attracted intensive attention in the field of solar cells because of their high conversion efficiencies.^{225–227} However, perovskite-type materials commonly used are Pb-based organic-inorganic hybrid compounds such as $\text{CH}_3\text{NH}_3\text{PbX}_3$ (X = Cl, Br, I). Although there has been no report on Mn-based perovskite-type materials benefiting from the non-toxic and high nature abundance, these series of alternatives are quite worthy of research.

The inherent low conductivity of most transition-metal oxides leads to their insulating or semiconducting character, which could not provide a high electronic conductivity as that in metal and carbon-based catalysts. To overcome this limitation, oxide materials are generally mechanically mixed with carbon powders to construct air electrodes. However, this method may not only limit the surface contact but also reduce the loading amount of the active samples. To combine an oxide catalyst with a highly conducting substrate (*e.g.*, carbon nanostructures) to form a composite is an alternative and useful strategy.^{189, 209, 210, 219, 228} Inorganic-nanocarbon hybrid could simultaneously enhance the electronic conductivity and improve the exposed distribution of active sites. The synergistic coupling effect in the hybrid enables better electrocatalytic performance than that of a single component. Cho's group²²⁹ has synthesized a composite air electrode consisting of KB carbon supported amorphous MnO_x nanowires. The high conductivity and large surface area of the MnO_x/KB composite along with the numerous defects contribute to the significantly improved ORR activity. The composite cathode based Zn–air batteries exhibit a peak power density of $\sim 190 \text{ mW cm}^{-2}$, which is far higher than that of commercial air Mn_3O_4 cathode and is similar to that of Pt-based catalyst. Other forms of carbon including graphene, carbon nanotubes/nanofibers, and porous carbon have also been selected as conductive matrix to support MnO_x nanostructures.^{210, 230–232} The hybrid cathode catalyst endows Li– O_2 batteries with low overvoltage and high capacity, suggesting their promising catalytic activity towards reversible discharge-charge reactions. Table 8 summarizes the synthetic method, capacitance, cyclability, and rate capability of several nanostructured Mn-base oxides as cathode catalysts for Li– O_2 batteries. The results encourage us to further promote the Li– O_2 batteries through designing new nanostructured Mn-base oxide catalysts.

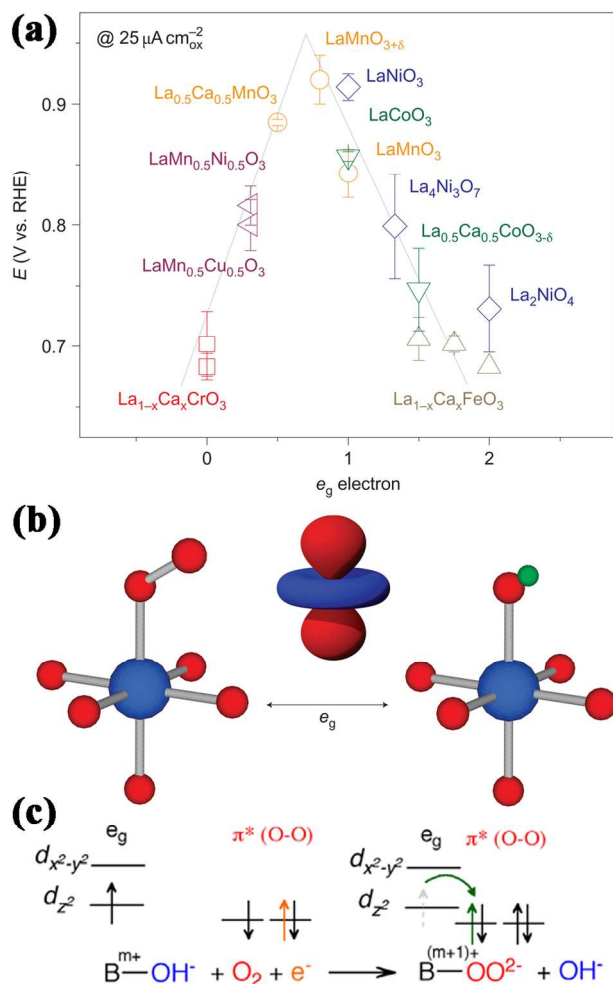


Fig. 15. (a) Potentials at 25 mA cm^{-2} as a function of e_g orbital in perovskite-based oxides. Data symbols vary with type of B ions. Error bars represent standard deviations. (b) The shape of the e_g electron points directly towards the surface O atom and plays an important role during $\text{O}_2^{2-}/\text{OH}^-$ exchange. (c) Proposed the mechanism of surface hydroxide displacement on perovskite oxide catalysts. Reproduced with permission from ref. 22, Copyright 2011, Nature Publishing Group.

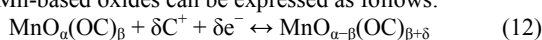
Table 8. Synthetic method, capacitance, cyclability, and rate capability of several nanostructured Mn-base oxides as cathode catalysts for Li- O_2 batteries.

Catalysts	Synthetic method	Maximum capacity based on total mass	Cycling performance/cutoff capacity	Rate capability	Ref.
α - MnO_2 nanowire	Hydrothermal method	730 mAh g^{-1} at 70 $\text{mA g}_{\text{carbon}}^{-1}$	10 cycles/2000 $\text{mAh g}_{\text{carbon}}^{-1}$	-	195
δ - $\text{MnO}_2/\text{Ni foam}$	Electrodeposition technique	7000 mAh g^{-1} at 100 mA g^{-1}	100 cycles/1000 mAh g^{-1}	1900 mAh g^{-1} at 800 mA g^{-1}	47
α - MnO_2 nanorods/Graphene composite	<i>In-situ</i> grown of α - MnO_2 nanorods on graphene nanosheets	2304 mAh g^{-1} at 200 $\text{mA g}_{\text{carbon}}^{-1}$	25 cycles/3000 mAh g^{-1}	-	210
α - MnO_2 nanorods/porous carbon composite	<i>In-situ</i> deposition of MnO_2 onto porous carbon	1400 mAh g^{-1} at 100 mA g^{-1}	60 cycles/500 mAh g^{-1}	-	231
Flower-like δ - $\text{MnO}_2/3\text{D}$ graphene composite	Hydrothermal method	3660 mAh g^{-1} at 48 mA g^{-1}	132 cycles/1000 mAh g^{-1}	770 mAh g^{-1} at 387 mA g^{-1}	233
Manganese oxide nanowire	Virus biotemplated method	5058 mAh g^{-1} at 40 mA g^{-1}	47 cycles/2000 $\text{mAh g}_{\text{carbon}}^{-1}$	-	212
$\text{MnCo}_2\text{O}_4/\text{graphene hybrid}$	Ethanol-water solvothermal method	3784 mAh g^{-1} at 100 mA g^{-1}	40 cycles/1000 mAh g^{-1}	2743 mAh g^{-1} at 800 mA g^{-1}	219
Porous CaMnO_3 nanostructure	Citric acid assisted sol-gel route	$\sim 3670 \text{ mAh g}^{-1}$ at 35 mA g^{-1}	80 cycles/500 $\text{mAh g}_{\text{carbon}}^{-1}$	$\sim 1830 \text{ mAh g}^{-1}$ at 105 mA g^{-1}	224
Porous $\text{La}_{0.75}\text{Sr}_{0.25}\text{MnO}_3$	Electrospinning	$\sim 11000 \text{ mAh}$	124 cycles/1000 mAh	$\sim 3890 \text{ mAh}$	222

nanotubes	technique with a heating method	g^{-1} at 16.7 mA g^{-1}	g^{-1}	g^{-1} at 133 mA g^{-1}
-----------	---------------------------------	------------------------------	----------	-----------------------------

5. Mn-based oxides as electrode materials for pseudocapacitors

Pseudocapacitors store the energy through either a fast or reversible redox reaction (Faradic reaction) on the electrode surface. The electrode materials of pseudocapacitors are usually transition metal oxides or polymer materials. The transition metal oxides display higher energy density than conventional carbon materials and better cycling performance than polymer materials.²⁴ Among various transition metal oxides, Mn-based oxides have attracted significant interest owing to their high specific capacitance, low price, natural abundance, and environmental friendliness. In 1991, Lee and Goodenough proposed the work principle of Mn-based oxides for pseudocapacitors.²³⁴ Afterwards, the charge storage mechanism in Mn-based oxide electrode is continuously improved. The Faradic reactions of Mn-based oxides can be expressed as follows:²⁴



where C^{+} represents the protons or alkali metal cations such as Li^{+} , Na^{+} , and K^{+} .

According to previous researches, crystallinity, crystal structure, morphology, and specific surface area are key factors to decide the performance of Mn-based oxides. High crystallinity is favourable toward enhancing the conductivity, but reduces the specific surface area. So choosing a suitable temperature of heat treatment is very important for the electrochemical performance of Mn-based oxides. Tsai's group²³⁵ prepared amorphous MnO_x nanofibers with mixture valences of Mn^{3+} and Mn^{4+} and investigated the effects of heat treatment on the performance. The sample annealed at 200 °C showed increased average oxidation state of Mn and the best cyclic stability. After annealing at 300 °C, the capacitive performance obviously decreased owing to morphology change. When the MnO_x was annealed above 500 °C, the pseudocapacitive behavior disappeared because of formation of crystalline Mn_2O_3 .

The MnO_x nanomaterials with different crystal structures also display varied performance. The amorphous $\alpha\text{-MnO}_2 \cdot n\text{H}_2\text{O}$ could exhibit a high specific capacitance of about 265–320 F g^{-1} .²³⁶ While, nanostructured $\alpha\text{-MnO}_2$ showed a specific capacitance of 168 F g^{-1} .²³⁷ Our group⁴⁷ used electrodeposition technique to prepare $\gamma\text{-MnO}_2$ nanoflake films with high specific capacitance of 240 F g^{-1} at 1 mA cm^{-2} , but the most reports on $\gamma\text{-MnO}_2$ materials only showed very low specific capacitances of 20–30 F g^{-1} .²³⁸ Donne *et al.*²³⁹ reported that birnessite-type $\delta\text{-MnO}_2$ prepared by hydrothermal method showed a specific capacitance of 150 F g^{-1} which is much higher than that of $\beta\text{-MnO}_2$ (25 F g^{-1}).

The nanostructures of MnO_x also have greatly effects on rate and cycling performance because the large specific surface area facilitates the improvement of specific capacitance. 0D MnO_2 nanoparticles prepared by electrodeposition showed a specific capacitance of 355 F g^{-1} at 20 mV s^{-1} .²⁴⁰ 1D MnO_2 nanotubes and nanowires exhibited good rate capability because the 1D nanostructures reduce the lengths of both electronic transport and ionic diffusion, leading to fast kinetics.²⁴¹ The specific capacitances of MnO_2 nanotube arrays are 349, 325, 285, and 245 F g^{-1} at current densities of 1, 2, 5, and 10 A g^{-1} , respectively. 2D H-type layered MnO_2 delivered a specific capacitance of 206 F g^{-1} at 5 mV s^{-1} ,²⁴² while 3D $\alpha\text{-MnO}_2$ nanoflower with a BET surface area of 206 $\text{m}^2 \text{g}^{-1}$ only displayed a low specific capacitance of 95 F g^{-1} at 2 mV s^{-1} .²⁴³

Poor electronic conductivity, low structural stability, and electrochemical dissolution of active materials are main problems for Mn-based oxides. One promising strategy to solve these problems is

the incorporation of nanostructured MnO_x into a conductive carbon matrix. Shao-Horn's group¹² prepared multiwall carbon nanotubes (MWNTs)/ MnO_2 nanocomposite by redox deposition of MnO_2 on layer-by-layer assembled MWNT films and the composite showed a high volumetric capacitance of 246 F cm^{-3} at 10 mV s^{-1} and ~11.6% decay after 1000 cycles at 200 mV s^{-1} (Fig. 16). Yan *et al.*²⁴⁴ reported graphene- MnO_2 composites with the specific capacitances of 310 F g^{-1} at 2 mV s^{-1} and 228 F g^{-1} at 500 mV s^{-1} . Shi and co-workers²⁴⁵ synthesized $\text{MnO}_2/\text{CMK-3}$ composite in which MnO_2 were embedded on the mesoporous carbon wall of CMK-3 materials rather than in their pores. The specific capacitance was over 200 F g^{-1} for $\text{MnO}_2/\text{CMK-3}$ composite and 600 F g^{-1} for the MnO_2 , and high cycling stability was obtained. Jiang *et al.*²⁴⁶ designed a novel one-dimensional structure combined with highly graphitic carbon, manganese oxide nanoparticles, mesoporous carbon, and manganese oxide nanowires. The unique structure significantly improved the conductivity of metal oxide materials and exhibited high specific capacitances of 266 F g^{-1} at 1 A g^{-1} and 150 F g^{-1} at 60 A g^{-1} . The specific capacitance almost had no decay after 1200 cycles at 50 mV s^{-1} . The energy densities of 20.8 Wh kg^{-1} was achieved at a power density of 30 kW kg^{-1} . Other conductive materials such as conductive polymers and metals can also improve the electrochemical utilization and promote the electrochemical stability. Ramaprabhu's group²⁴⁷ reported an *in-situ* polymerization method to synthesize the nanocomposite based on polyaniline (PANI) and MnO_2 nanotubes. The PANI- MnO_2 composite showed a specific capacitance of 626 F g^{-1} at 2 A g^{-1} , corresponding to the energy density of 17.8 Wh kg^{-1} . Xia's group²⁴⁸ fabricated hierarchical Ti@MnO_2 nanowire arrays with specific capacitances of 468 F g^{-1} at 1 A g^{-1} and 311 F g^{-1} at 20 A g^{-1} .

Table 9 lists the synthetic method, capacitance, cyclability, and rate capability of several nanostructured Mn-base oxides. $\text{MnO}_2/\text{conductive material}$ nanocomposites exhibit higher performance than bare MnO_2 , but it is still lower than the theoretical specific capacitance of MnO_2 (1370 F g^{-1}) and practical specific capacitance of RuO_2 (600–1200 F g^{-1}).²⁴ Therefore, nanostructured Mn-base oxides have a great potential for further development.

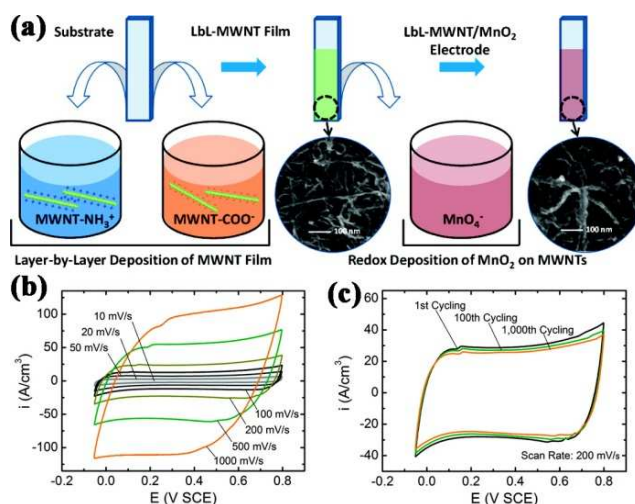


Fig. 16. (a) Schematic illustration of synthetic method of MWNTs/ MnO_2 nanocomposite. (b) Rate-dependent cyclic voltammograms of MWNT/ MnO_2 electrodes at various scan rates from 10 to 1000 mV s^{-1} . (c) Cyclic voltammograms obtained from MWNT/ MnO_2 electrodes with different cycling numbers at a scan

rate of 200 mV s⁻¹. Reproduced with permission from ref. 12, Copyright 2010, American Chemical Society.

Table 9. Synthetic method, capacitance, cyclability, and rate capability of several nanostructured Mn-base oxides as electrode materials of pseudocapacitors.

Materials	Synthetic method	Capacitance	Capacity retention	Rate capability	Ref.
γ -MnO ₂ nanoflake films	Electrodeposition technique	285 F g ⁻¹ at 0.1 mA cm ⁻²	-	240 F g ⁻¹ at 1 mA cm ⁻²	47
MnO ₂ nanotube array	Template assisted-electrodeposition technique	349 F g ⁻¹ at 1 A g ⁻¹	81% after 2000 cycles at 2 A g ⁻¹	245 F g ⁻¹ at 10 A g ⁻¹	241
MnO ₂ /Multiwall carbon nanotube (MWNT) nanocomposite	Redox deposition of MnO ₂ on layer-by-layer assembled MWNT films	246 F g ⁻¹ at 10 mV s ⁻¹	88.4% after 1000 cycles at 200 mV s ⁻¹	~120 F g ⁻¹ at 1000 mV s ⁻¹	12
MnO ₂ /vertically aligned carbon nanotube composite	Electrodeposition technique	642 F g ⁻¹ at 10 mV s ⁻¹	>80% after 800 cycles at 1 mA cm ⁻²	~400 F g ⁻¹ at 150 mV s ⁻¹	249
MnO ₂ /mesoporous carbon composite	Redox reaction between permanganate ions and carbons	220 F cm ⁻³ at 5 mV s ⁻¹	92% after 1000 cycles at 5 mV s ⁻¹	156 F cm ⁻³ at 50 mV s ⁻¹	245
MnO ₂ /rGO composite	Self-limiting deposition of nanoscale MnO ₂ on the surface of graphene under microwave irradiation	310 F g ⁻¹ at 2 mV s ⁻¹	95.4% after 15000 cycles at 500 mV s ⁻¹	228 F g ⁻¹ at 500 mV s ⁻¹	244
Highly graphitic carbon-tipped MnO _x nanoparticles/mesoporous carbon/MnO _x nanowires	Multistep reaction	266 F g ⁻¹ at 1 A g ⁻¹	>100% after 1200 cycles at 50 mV s ⁻¹	150 F g ⁻¹ at 60 A g ⁻¹	246
MnO ₂ nanotube/polyaniline nanocomposite	<i>In-situ</i> polymerization	626 F g ⁻¹ at 2 A g ⁻¹	~90% after 1000 cycles at 10 A g ⁻¹	480 F cm ⁻³ at 20 A g ⁻¹	247
MnO ₂ @Ti nanowire arrays	Hydrothermal method	468 F g ⁻¹ at 1 A g ⁻¹	96.8% after 5000 cycles at 5 A g ⁻¹	311 F g ⁻¹ at 20 A g ⁻¹	248

In the past 100 years, the science and technology of electrochemical energy storage and conversion have continuously developed. Batteries and capacitors have been widely used in people's daily life. For the batteries with a closed system (*e.g.*, Zn–MnO₂ batteries and rechargeable LIBs), the electrochemical reaction is an ionic insertion/deintercalation reaction which takes place on the interface between the solid active materials and liquid electrolyte, while for the batteries with an open system (*e.g.*, metal–air batteries like Li–O₂ batteries and fuel cells), the redox reaction usually takes place on the interface among the solid catalysts, liquid electrolyte, and gas cathode material (*i.e.*, O₂) with a normally three-phase

reaction. Recently, pseudocapacitors are particularly attractive because of their battery-level energy density and EDLC-degree power density.²⁶ Fig. 17 describes the applications of Mn-based oxides for electrochemical energy storage and conversion over the years, including 1D nanostructured γ -MnO₂ as the cathode of primary Zn–MnO₂ batteries, porous spinel-type LiNi_{0.5}Mn_{1.5}O₄ nanorods as the cathodes of LIBs, perovskite-type CaMnO₃ as ORR or OER catalysts of rechargeable Li–air batteries, and MnO₂ as the electrode materials of pseudocapacitors. Notably, metal–air batteries and pseudocapacitors would be most likely to be developed in the future.

ARTICLE

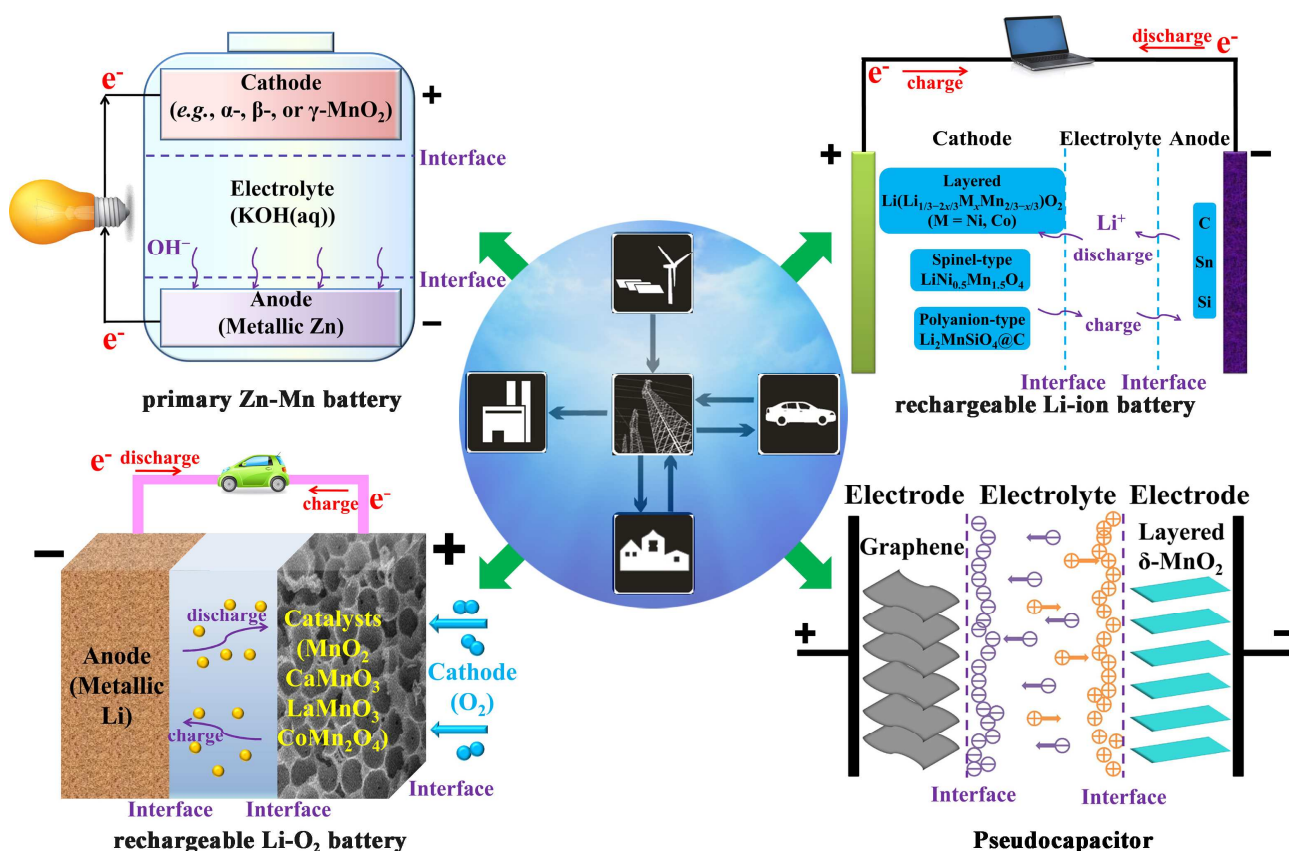


Fig. 17. Applications of the Mn-based oxides for electrochemical energy storage and conversion over the years.

6. Conclusions and outlook

A series of Mn-based oxides with different nanostructures have been applied as the electrode materials of primary batteries, LIBs, pseudocapacitors, and electrocatalysts of rechargeable Li–O₂ batteries. This is due to their native advantages of inexpensive price, high abundance, acceptable activity, and low toxicity in comparison with traditional bulk electrode materials and noble metal based catalysts. The influence of structure, morphology, and composition on the electrochemical performance has been widely studied. Generally, nanostructures can promote the electrochemical reaction occurring at the solid–liquid or solid–liquid–gas interface to obtain high energy density. Furthermore, nanomaterials facilitate both electronic and ionic transport, leading to excellent rate performance. Thus, it is that nanostructured materials improve the thermodynamics and kinetics properties of electrochemical reactions for achieving high energy and power density.

For primary batteries, the low specific capacity of Zn–MnO₂ and Li–MnO₂ batteries is difficult to achieve long-life use. Mg–air, Al–air, and Zn–air batteries have large specific capacity, but the alkaline electrolyte suffers the difficulties of the leakage, evaporation, hygroscopicity, and reaction with CO₂ limiting the scalable application. Using quasi-solid-state or solid-state electrolytes

combined with nanostructured Mn-based oxides as catalysts may become future research direction.

For LIBs, layered, spinel-type, and polyanion-type Mn-based oxides have different features. Layered Li-rich Mn-based oxides exhibit high specific capacity of ~ 300 mAh g⁻¹, but low initial Coulombic efficiency, sluggish Li⁺ ion diffusion, and poor cycling stability obstacle their application. Although the surface coating and core-shell structure relieve these problems in some degree, their internal phase transformation cannot be absolutely avoided. Doping other cations combined with concentration-gradient structure is helpful to improve the structure stability and reaction kinetics. Spinel-type LiNi_{0.5}Mn_{1.5}O₄ possesses fast 3D Li⁺ diffusion path and high operational potential (~ 4.7 V vs. Li⁺/Li), but the stability of electrolyte and active materials at high potential is difficult to guarantee. Using 1D porous structure with surface coating would shed light on developing high potential cathode materials for advanced LIBs. Polyanion-type Li₂MnSiO₄ can achieve 2e⁻ reaction with high specific capacity of ~ 333 mAh g⁻¹, but suffers from low conductivity and poor stability. Core-shell structured Li₂MnSiO₄@C nanocomposites have great improvements on the rate and cycling performance. However, no obvious effort for optimizing the operation voltage of Li₂MnSiO₄ is observed. To obtain high energy and power density, further attempts should

focus on the modification of ion doping such as Co^{2+} and Ni^{2+} at Mn site or PO_4^{3-} , TiO_4^{4-} , and AlO_3^{3-} at anion site.

For rechargeable metal–air batteries, extensive fundamental studies about the catalytic mechanism and the correlation between the electrochemical performance and physicochemical properties are urgent. A combination of theoretical calculation and *in-situ* experimental analysis would be helpful to gain the in-depth insights. Apart from these, functional materials critically determine the characteristics of assembled electrochemical devices. As for metal–air systems, the sluggish kinetics of oxygen reduction/evolution requires the highly efficient bifunctional active catalysts. Mn-based oxides along with various favorable nanostructures are particularly attractive and have been intensely investigated as non-precious catalysts in both aqueous and nonaqueous systems accompanied with different mechanisms. Compared to discharge processes (*i.e.*, ORR), the catalytic behavior for charge is more challenging in rechargeable metal–air batteries, especially in Li–air systems owing to the electrochemical decomposition of the discharge products (*i.e.*, Li_2O_2). This leads to large anodic polarization and limited cycling ability. Efficient electrocatalysts are urgently required to promote the reversible formation-decomposition of Li_2O_2 and to lower the overpotential for avoiding carbon corrosion and electrolyte oxidation. By tailoring the physicochemical parameters of the catalysts (*e.g.*, composition, valence value, phase, structure, defect, morphology, size, surface area, and conductivity), improved intrinsic catalytic activity and enhanced density and utilization of the active sites could be obtained through optimizing synthesis strategies and conditions. In addition, rational structure including hierarchical porosity facilitating ion and O_2 diffusion and transport and the uniform catalyst distribution also contributes to the improvement of electrode/battery performance. Furthermore, Nature may aid in exploiting and developing new electrocatalysts. Mimicking natural oxygen catalytic processes would help to search for better catalysts.

Pseudocapacitors are particularly attractive because of their battery-level energy density and EDLC-degree power density. MnO_2 has a theoretical specific capacitance of 1370 F g^{-1} , but its practical specific capacitance is lower than 400 F g^{-1} . Furthermore, MnO_2 suffers from poor electronic conductivity, low structural stability, and electrochemical dissolution. MnO_2 /conductive material nanocomposites obviously improve the performance, but the full potential of MnO_2 -based pseudocapacitors has not been explored. Using porous MnO_2 /conductive material composites with large surface area combined with optimum electrolyte and separators would make pseudocapacitors more attractive.

It is noted that future studies of Mn-based oxides with nanostructures should focus on achieving the large scale preparation, increasing the tap density and volumetric energy density, and maintaining the high electrochemical performance. To sum up the present research efforts and progress, great opportunities and huge challenges coexist in this field.

Acknowledgements

This work was supported by the Programs of National 973 (2011CB935900), NSFC (21231005 and 51231003), MOE (113016A, B12015 and IRT13R30), and Tianjin High-Tech (12ZCZDJC35300).

Notes and references

Key Laboratory of Advanced Energy Materials Chemistry (Ministry of Education), Collaborative Innovation Center of Chemical Science and

Engineering, College of Chemistry, Nankai University, Tianjin 300071, China

Address correspondence to chenabc@nankai.edu.cn

1. B. Dunn, H. Kamath and J.-M. Tarascon, *Science*, 2011, **334**, 928–935.
2. Q. Zhang, E. Uchaker, S. L. Candelaria and G. Cao, *Chem. Soc. Rev.*, 2013, **42**, 3127–3171.
3. Z. Yang, J. Zhang, M. C. W. Kintner-Meyer, X. Lu, D. Choi, J. P. Lemmon and J. Liu, *Chem. Rev.*, 2011, **111**, 3577–3613.
4. F. Cheng and J. Chen, *Chem. Soc. Rev.*, 2012, **41**, 2172–2192.
5. F. Cheng, J. Liang, Z. Tao and J. Chen, *Adv. Mater.*, 2011, **23**, 1695–1715.
6. M. S. Islam and C. A. J. Fisher, *Chem. Soc. Rev.*, 2014, **43**, 185–204.
7. W. Wei, X. Cui, W. Chen and D. G. Ivey, *Chem. Soc. Rev.*, 2011, **40**, 1697–1721.
8. S. L. Suib, *Acc. Chem. Res.*, 2008, **41**, 479–487.
9. Z. Chen, Z. Jiao, D. Pan, Z. Li, M. Wu, C.-H. Shek, C. M. L. Wu and J. K. L. Lai, *Chem. Rev.*, 2012, **112**, 3833–3855.
10. W. M. Haynes, *Handbook of Chemistry and Physics (93rd edn)*, CRC Press, 2012–2013.
11. F. Cheng, J. Chen, X. Gou and P. Shen, *Adv. Mater.*, 2005, **17**, 2753–2756.
12. S. W. Lee, J. Kim, S. Chen, P. T. Hammond and Y. Shao-Horn, *ACS Nano*, 2010, **4**, 3889–3896.
13. F. Cheng, H. Wang, Z. Zhu, Y. Wang, T. Zhang, Z. Tao and J. Chen, *Energy Environ. Sci.*, 2011, **4**, 3668–3675.
14. J. Yang, X. Han, X. Zhang, F. Cheng and J. Chen, *Nano Res.*, 2013, **6**, 679–687.
15. X. Han, T. Zhang, J. Du, F. Cheng and J. Chen, *Chem. Sci.*, 2013, **4**, 368–376.
16. M. Winter and R. J. Brodd, *Chem. Rev.*, 2004, **104**, 4245–4270.
17. J. Chen and F. Cheng, *Acc. Chem. Res.*, 2009, **42**, 713–723.
18. Y. Wang, H. Li, P. He, E. Hosono and H. Zhou, *Nanoscale*, 2010, **2**, 1294–1305.
19. F. Jiao and P. G. Bruce, *Adv. Mater.*, 2007, **19**, 657–660.
20. Z. Hu, K. Zhang, H. Gao, W. Duan, F. Cheng, J. Liang and J. Chen, *J. Mater. Chem. A*, 2013, **1**, 12650–12656.
21. F. Cheng, J. Shen, B. Peng, Y. Pan, Z. Tao and J. Chen, *Nat. Chem.*, 2011, **3**, 79–84.
22. J. Suntivich, H. A. Gasteiger, N. Yabuuchi, H. Nakanishi, J. B. Goodenough and Y. Shao-Horn, *Nat. Chem.*, 2011, **3**, 546–550.
23. X. Han, F. Cheng, T. Zhang, J. Yang, Y. Hu and J. Chen, *Adv. Mater.*, 2014, **26**, 2047–2051.
24. G. Wang, L. Zhang and J. Zhang, *Chem. Soc. Rev.*, 2012, **41**, 797–828.
25. P. J. Hall, M. Mirzaeian, S. I. Fletcher, F. B. Sillars, A. J. R. Rennie, G. O. Shitta-Bey, G. Wilson, A. Cruden and R. Carter, *Energy Environ. Sci.*, 2010, **3**, 1238–1251.
26. P. Simon, Y. Gogotsi and B. Dunn, *Science*, 2014, **343**, 1210–1211.
27. A. J. Bard and L. R. Faulkner, *Electrochemical Methods Fundamentals and Applications*, John Wiley & Sons, 2003.
28. E. Barsoukov and J. R. Macdonald, *Impedance Spectroscopy Theory, Experiment, and Applications*, John Wiley & Sons, 2005.
29. A. S. Arico, P. Bruce, B. Scrosati, J.-M. Tarascon and W. van Schalkwijk, *Nat. Mater.*, 2005, **4**, 366–377.
30. P. G. Bruce, B. Scrosati and J.-M. Tarascon, *Angew. Chem. Int. Ed.*, 2008, **47**, 2930–2946.

31. J. Maier, *Nat. Mater.*, 2005, **4**, 805–815.
32. S. Xin, Y. Guo and L. Wan, *Acc. Chem. Res.*, 2012, **45**, 1759–1769.
33. M.-H. Park, M. G. Kim, J. Joo, K. Kim, J. Kim, S. Ahn, Y. Cui and J. Cho, *Nano Lett.*, 2009, **9**, 3844–3847.
34. S. Cavaliere, S. Subianto, I. Savych, D. J. Jones and J. Roziere, *Energy Environ. Sci.*, 2011, **4**, 4761–4785.
35. S. Liu, S. Sun and X. You, *Nanoscale*, 2014, **6**, 2037–2045.
36. J. Xiao, J. Zheng, X. Li, Y. Shao and J. Zhang, *Nanotechnology*, 2013, **24**, 424004.
37. X. Lou, L. A. Archer and Z. Yang, *Adv. Mater.*, 2008, **20**, 3987–4019.
38. X. Wang and Y. Li, *J. Am. Chem. Soc.*, 2002, **124**, 2880–2881.
39. F. Cheng, J. Zhao, W. Song, C. Li, H. Ma, J. Chen and P. Shen, *Inorg. Chem.*, 2006, **45**, 2038–2044.
40. J. Zhao, Z. Tao, J. Liang and J. Chen, *Cryst. Growth Des.*, 2008, **8**, 2799–2805.
41. X. Hu, X. Han, Y. Hu, F. Cheng and J. Chen, *Nanoscale*, 2014, **6**, 3522–3525.
42. W. Zhou, *J. Mater. Chem.*, 2008, **18**, 5321–5325.
43. Z. Yuan, Z. Zhang, G. Du, T. Ren and B. Su, *Chem. Phys. Lett.*, 2003, **378**, 349–353.
44. Q. Zhou, X. Li, Y. Li, B. Tian, D. Zhao and Z. Jiang, *Chinese J. Chem.*, 2006, **24**, 835–839.
45. C. Li, F. Cheng, W. Ji, Z. Tao and J. Chen, *Nano Res.*, 2009, **2**, 713–721.
46. F. Cheng, Y. Su, J. Liang, Z. Tao and J. Chen, *Chem. Mater.*, 2010, **22**, 898–905.
47. S. Chou, F. Cheng and J. Chen, *J. Power Sources*, 2006, **162**, 727–734.
48. Z. Yang, J. Liang, F. Cheng, Z. Tao and J. Chen, *Microporous Mesoporous Mater.*, 2012, **161**, 40–47.
49. B. Xin, W. Jiang, X. Li, K. Zhang, C. Liu, R. Wang and Y. Wang, *Bioresour. Technol.*, 2012, **112**, 186–192.
50. H. Ma, C. Li, Y. Su and J. Chen, *J. Mater. Chem.*, 2007, **17**, 684–691.
51. A. Bahloul, B. Nessark, N. E. Chelali, H. Groult, A. Mauger and C. M. Julien, *Solid State Ionics*, 2011, **204–205**, 53–60.
52. M. Sugantha, P. A. Ramakrishnan, A. M. Hermann, C. P. Warmsingh and D. S. Ginley, *Int. J. Hydrogen Energy*, 2003, **28**, 597–600.
53. N. Kijima, Y. Takahashi, J. Akimoto and J. Awaka, *J. Solid State Chem.*, 2005, **178**, 2741–2750.
54. S. Jouanneau, S. Sarciaux, A. Le Gal La Salle and D. Guyomard, *Solid State Ionics*, 2001, **140**, 223–232.
55. W. M. Dose and S. W. Donne, *Journal of Power Sources*, 2013, **221**, 261–265.
56. W. M. Dose and S. W. Donne, *Electrochim. Acta*, 2013, **105**, 305–313.
57. W. M. Dose and S. W. Donne, *J. Power Sources*, 2014, **247**, 852–857.
58. Q. Liu, S. Wang and H. Cheng, *Int. J. Electrochem. Sci.*, 2013, **8**, 10540–10548.
59. S. Wang, Q. Liu, J. Yu and J. Zeng, *Int. J. Electrochem. Sci.*, 2012, **7**, 1242–1250.
60. J. Read, A. Driedger, D. Foster, J. Wolfenstine and W. Behl, *Electrochim. Solid State Lett.*, 2001, **4**, A162–A165.
61. S. R. Srither, M. Selvam, S. Arunmetha, R. Yuvakkumar, K. Saminathan and V. Rajendran, *Sci. Adv. Mater.*, 2013, **5**, 1372–1376.
62. K. J. Ramalingam and S. R. Srither, 2013 International Conference on Power, Energy and Control (ICPEC), *IEEE*, 2013, 788–791.
63. M. R. Palacin, *Chem. Soc. Rev.*, 2009, **38**, 2565–2575.
64. J. B. Goodenough and Y. Kim, *Chem. Mater.*, 2009, **22**, 587–603.
65. Y. Sun, X. Hu, W. Luo, F. Xia and Y. Huang, *Adv. Funct. Mater.*, 2013, **23**, 2436–2444.
66. X. Zhang, F. Cheng, J. Yang and J. Chen, *Nano Lett.*, 2013, **13**, 2822–2825.
67. N. Yabuuchi, K. Yoshii, S.-T. Myung, I. Nakai and S. Komaba, *J. Am. Chem. Soc.*, 2011, **133**, 4404–4419.
68. D. Zeng, J. Cabana, W.-S. Yoon and C. P. Grey, *Chem. Mater.*, 2010, **22**, 1209–1219.
69. S. Aono, T. Tsurudo, K. Urita and I. Moriguchi, *Chem. Commun.*, 2013, **49**, 2939–2941.
70. H. Wang, L. Cui, Y. Yang, H. Sanchez Casalongue, J. T. Robinson, Y. Liang, Y. Cui and H. Dai, *J. Am. Chem. Soc.*, 2010, **132**, 13978–13980.
71. H. Jiang, Y. Hu, S. Guo, C. Yan, P. S. Lee and C. Li, *ACS Nano*, 2014, **8**, 6038–6046.
72. T.-J. Kim, D. Son, J. Cho and B. Park, *J. Power Sources*, 2006, **154**, 268–272.
73. S. B. Schougaard, J. Bréger, M. Jiang, C. P. Grey and J. B. Goodenough, *Adv. Mater.*, 2006, **18**, 905–909.
74. N. N. Sinha and N. Munichandraiah, *J. Electrochem. Soc.*, 2010, **157**, A647–A653.
75. H. Yu and H. Zhou, *J. Phys. Chem. Lett.*, 2013, **4**, 1268–1280.
76. D. Choi, D. Wang, I.-T. Bae, J. Xiao, Z. Nie, W. Wang, V. V. Viswanathan, Y. J. Lee, J.-G. Zhang, G. L. Graff, Z. Yang and J. Liu, *Nano Lett.*, 2010, **10**, 2799–2805.
77. X. Yu, Y. He, J. Sun, K. Tang, H. Li, L. Chen and X. Huang, *Electrochim. Commun.*, 2009, **11**, 791–794.
78. K. Zhong, B. Zhang, S. Luo, W. Wen, H. Li, X. Huang and L. Chen, *J. Power Sources*, 2011, **196**, 6802–6808.
79. X. Li, D. Li, L. Qiao, X. Wang, X. Sun, P. Wang and D. He, *J. Mater. Chem.*, 2012, **22**, 9189–9194.
80. Y. Ding, C. Wu, H. Yu, J. Xie, G. Cao, T. Zhu, X. Zhao and Y. Zeng, *Electrochim. Acta*, 2011, **56**, 5844–5848.
81. B. Sun, Z. Chen, H.-S. Kim, H. Ahn and G. Wang, *J. Power Sources*, 2011, **196**, 3346–3349.
82. L. Su, Y. Zhong, J. Wei and Z. Zhou, *RSC Adv.*, 2013, **3**, 9035–9041.
83. Y. Mai, D. Zhang, Y. Qiao, C. Gu, X. Wang and J. Tu, *J. Power Sources*, 2012, **216**, 201–207.
84. Y. Sun, X. Hu, W. Luo and Y. Huang, *J. Mater. Chem.*, 2012, **22**, 19190–19195.
85. X. Zhang, Z. Xing, L. Wang, Y. Zhu, Q. Li, J. Liang, Y. Yu, T. Huang, K. Tang, Y. Qian and X. Shen, *J. Mater. Chem.*, 2012, **22**, 17864–17869.
86. P. He, H. Yu, D. Li and H. Zhou, *J. Mater. Chem.*, 2012, **22**, 3680–3695.
87. E. Rossen, C. D. W. Jones and J. R. Dahn, *Solid State Ionics*, 1992, **57**, 311–318.
88. Y. Makimura and T. Ohzuku, *J. Power Sources*, 2003, **119–121**, 156–160.
89. M. S. Islam, R. A. Davies and J. D. Gale, *Chem. Mater.*, 2003, **15**, 4280–4286.
90. Y. Koyama, Y. Makimura, I. Tanaka, H. Adachi and T. Ohzuku, *J. Electrochem. Soc.*, 2004, **151**, A1499–A1506.
91. Y.-K. Sun, S.-T. Myung, B.-C. Park and H. Yashiro, *J. Electrochem. Soc.*, 2008, **155**, A705–A710.
92. H. Liu, Y. Hu, Y. Li and H. Gu, *Mater. Chem. Phys.*, 2013, **138**, 440–443.
93. Y. Liu, B. Chen, F. Cao, X. Zhao and J. Yuan, *J. Mater. Chem.*, 2011, **21**, 10437–10441.

94. D. H. Park, S. T. Lim, S. J. Hwang, C. S. Yoon, Y. K. Sun and J. H. Choy, *Adv. Mater.*, 2005, **17**, 2834–2837.
95. Z. Li, N. A. Chernova, M. Roppolo, S. Upreti, C. Petersburg, F. M. Alamgir and M. S. Whittingham, *J. Electrochem. Soc.*, 2011, **158**, A516–A522.
96. M.-H. Kim, H.-S. Shin, D. Shin and Y.-K. Sun, *J. Power Sources*, 2006, **159**, 1328–1333.
97. Y.-K. Sun, S.-T. Myung, M.-H. Kim, J. Prakash and K. Amine, *J. Am. Chem. Soc.*, 2005, **127**, 13411–13418.
98. Y.-K. Sun, S.-T. Myung, B.-C. Park, J. Prakash, I. Belharouak and K. Amine, *Nat. Mater.*, 2009, **8**, 320–324.
99. T. Ohzuku and Y. Makimura, *Chem. Lett.*, 2001, 642–643.
100. N. Yabuuchi, Y. Koyama, N. Nakayama and T. Ohzuku, *J. Electrochem. Soc.*, 2005, **152**, A1434–A1440.
101. L. Du, H. Ren and Z. Peng, *Mater. Chem. Phys.*, 2012, **135**, 264–267.
102. C. Yang, J. Huang, L. Huang and G. Wang, *J. Power Sources*, 2013, **226**, 219–222.
103. Y. Yao, H. Liu, G. Li, H. Peng and K. Chen, *Electrochim. Acta*, 2013, **113**, 340–345.
104. H. G. Song, J. Y. Kim and Y. J. Park, *Electrochim. Acta*, 2011, **56**, 6896–6905.
105. S. Shi, J. Tu, Y. Tang, Y. Zhang, X. Liu, X. Wang and C. Gu, *J. Power Sources*, 2013, **225**, 338–346.
106. C. Gong, W. Lv, L. Qu, O. E. Bankole, G. Li, R. Zhang, M. Hu and L. Lei, *J. Power Sources*, 2014, **247**, 151–155.
107. F. Wu, M. Wang, Y. Su, L. Bao and S. Chen, *J. Power Sources*, 2010, **195**, 2900–2904.
108. F. Fu, G. Xu, Q. Wang, Y. Deng, X. Li, J. Li, L. Huang and S. Sun, *J. Mater. Chem. A*, 2013, **1**, 3860–3864.
109. J. Lu, Q. Peng, W. Wang, C. Nan, L. Li and Y. Li, *J. Am. Chem. Soc.*, 2013, **135**, 1649–1652.
110. J. Liu, M. Hou, J. Yi, S. Guo, C. Wang and Y. Xia, *Energy Environ. Sci.*, 2014, **7**, 705–714.
111. J. Yang, F. Cheng, X. Zhang, H. Gao, Z. Tao and J. Chen, *J. Mater. Chem. A*, 2014, **2**, 1636–1640.
112. Y. Kim, Y. Hong, M. G. Kim and J. Cho, *Electrochem. Commun.*, 2007, **9**, 1041–1046.
113. M. G. Kim, M. Jo, Y.-S. Hong and J. Cho, *Chem. Commun.*, 2009, 218–220.
114. J. Liu, L. Chen, M. Hou, F. Wang, R. Che and Y. Xia, *J. Mater. Chem.*, 2012, **22**, 25380–25387.
115. Y. Lee, M. G. Kim and J. Cho, *Nano Lett.*, 2008, **8**, 957–961.
116. Y. Jiang, Z. Yang, W. Luo, X. Hu and Y. Huang, *Phys. Chem. Chem. Phys.*, 2013, **15**, 2954–2960.
117. J. Liu and A. Manthiram, *J. Mater. Chem.*, 2010, **20**, 3961–3967.
118. Q. Wang, J. Liu, A. V. Murugan and A. Manthiram, *J. Mater. Chem.*, 2009, **19**, 4965–4972.
119. M. M. Thackeray, W. I. F. David, P. G. Bruce and J. B. Goodenough, *Mater. Res. Bull.*, 1983, **18**, 461–472.
120. M. M. Thackeray, P. J. Johnson, L. A. de Picciotto, P. G. Bruce and J. B. Goodenough, *Mater. Res. Bull.*, 1984, **19**, 179–187.
121. T. Ohzuku, M. Kitagawa and T. Hirai, *J. Electrochem. Soc.*, 1990, **137**, 769–775.
122. J. M. Tarascon and D. Guyomard, *J. Electrochem. Soc.*, 1991, **138**, 2864–2868.
123. J. M. Tarascon, E. Wang, F. K. Shokoohi, W. R. McKinnon and S. Colson, *J. Electrochem. Soc.*, 1991, **138**, 2859–2864.
124. M. M. Thackeray, *Prog. Solid State Chem.*, 1997, **25**, 1–71.
125. M. Yonemura, A. Yamada, H. Kobayashi, M. Tabuchi, T. Kamiyama, Y. Kawamoto and R. Kanno, *J. Mater. Chem.*, 2004, **14**, 1948–1958.
126. D. Aurbach, M. D. Levi, K. Gamulski, B. Markovsky, G. Salitra, E. Levi, U. Heider, L. Heider and R. Oesten, *J. Power Sources*, 1999, **81–82**, 472–479.
127. W. Liu, K. Kowal and G. C. Farrington, *J. Electrochem. Soc.*, 1998, **145**, 459–465.
128. D. Guan, J. A. Jeevarajan and Y. Wang, *Nanoscale*, 2011, **3**, 1465–1469.
129. J. S. Gnanaraj, V. G. Pol, A. Gedanken and D. Aurbach, *Electrochem. Commun.*, 2003, **5**, 940–945.
130. L. Hernan, J. Morales, L. Sanchez, E. R. Castellon and M. A. G. Aranda, *J. Mater. Chem.*, 2002, **12**, 734–741.
131. L. Xiong, Y. Xu, T. Tao, J. Song and J. B. Goodenough, *J. Mater. Chem.*, 2012, **22**, 24563–24568.
132. F. Jiao, J. Bao, A. H. Hill and P. G. Bruce, *Angew. Chem. Int. Ed.*, 2008, **47**, 9711–9716.
133. D. K. Kim, P. Muralidharan, H.-W. Lee, R. Ruffo, Y. Yang, C. K. Chan, H. Peng, R. A. Huggins and Y. Cui, *Nano Lett.*, 2008, **8**, 3948–3952.
134. Y. Wang, Y. Wang, D. Jia, Z. Peng, Y. Xia and G. Zheng, *Nano Lett.*, 2014, **14**, 1080–1084.
135. B. J. Liddle, S. M. Collins and B. M. Bartlett, *Energy Environ. Sci.*, 2010, **3**, 1339–1346.
136. Y. Ding, J. Xie, G. Cao, T. Zhu, H. Yu and X. Zhao, *Adv. Funct. Mater.*, 2011, **21**, 348–355.
137. K. M. Shaju and P. G. Bruce, *Chem. Mater.*, 2008, **20**, 5557–5562.
138. E. Hosono, T. Kudo, I. Honma, H. Matsuda and H. Zhou, *Nano Lett.*, 2009, **9**, 1045–1051.
139. C. Jiang, S. Dou, H. Liu, M. Ichihara and H. Zhou, *J. Power Sources*, 2007, **172**, 410–415.
140. J. Luo, Y. Wang, H. Xiong and Y. Xia, *Chem. Mater.*, 2007, **19**, 4791–4795.
141. Q. Qu, L. Fu, X. Zhan, D. Samuelis, J. Maier, L. Li, S. Tian, Z. Li and Y. Wu, *Energy Environ. Sci.*, 2011, **4**, 3985–3990.
142. S.-M. Bak, K.-W. Nam, C.-W. Lee, K.-H. Kim, H.-C. Jung, X.-Q. Yang and K.-B. Kim, *J. Mater. Chem.*, 2011, **21**, 17309–17315.
143. S. Lee, Y. Cho, H.-K. Song, K. T. Lee and J. Cho, *Angew. Chem. Int. Ed.*, 2012, **51**, 8748–8752.
144. S. Lee, M. Jeong and J. Cho, *Adv. Energy Mater.*, 2013, **3**, 1623–1629.
145. O. K. Park, Y. Cho, S. Lee, H.-C. Yoo, H.-K. Song and J. Cho, *Energy Environ. Sci.*, 2011, **4**, 1621–1633.
146. K. Amine, H. Tukamoto, H. Yasuda and Y. Fujita, *J. Electrochem. Soc.*, 1996, **143**, 1607–1613.
147. K. Amine, H. Tukamoto, H. Yasuda and Y. Fujita, *J. Power Sources*, 1997, **68**, 604–608.
148. Y. Gao, K. Myrtle, M. Zhang, J. N. Reimers and J. R. Dahn, *Phys. Rev. B*, 1996, **54**, 16670–16675.

149. J. Cabana, M. Casas-Cabanas, F. O. Omenya, N. A. Chernova, D. Zeng, M. S. Whittingham and C. P. Grey, *Chem. Mater.*, 2012, **24**, 2952–2964.
150. J. H. Kim, S. T. Myung, C. S. Yoon, S. G. Kang and Y. K. Sun, *Chem. Mater.*, 2004, **16**, 906–914.
151. N. Amdouni, K. Zaghbi, F. Gendron, A. Mauger and C. M. Julien, *Ionics*, 2006, **12**, 117–126.
152. X. Ma, B. Kang and G. Ceder, *J. Electrochem. Soc.*, 2010, **157**, A925–A931.
153. K. M. Shaju and P. G. Bruce, *Dalton Trans.*, 2008, 5471–5475.
154. M. Kunduraci, J. F. Al-Sharab and G. G. Amatucci, *Chem. Mater.*, 2006, **18**, 3585–3592.
155. J. Yang, X. Zhang, Z. Zhu, F. Cheng and J. Chen, *J. Electroanal. Chem.*, 2013, **688**, 113–117.
156. X. Zhang, F. Cheng, K. Zhang, Y. Liang, S. Yang, J. Liang and J. Chen, *RSC Adv.*, 2012, **2**, 5669–5675.
157. L. Zhou, D. Zhao and X. Lou, *Angew. Chem. Int. Ed.*, 2012, **51**, 239–241.
158. S. Yang, T. Zhang, Z. Tao and J. Chen, *Acta Chim. Sin.*, 2013, **71**, 1029–1034.
159. M.-C. Yang, B. Xu, J.-H. Cheng, C.-J. Pan, B.-J. Hwang and Y. S. Meng, *Chem. Mater.*, 2011, **23**, 2832–2841.
160. D. W. Shin, C. A. Bridges, A. Huq, M. P. Paranthaman and A. Manthiram, *Chem. Mater.*, 2012, **24**, 3720–3731.
161. J. Yang, X. Zhang, X. Han, F. Cheng, Z. Tao and J. Chen, *J. Mater. Chem. A*, 2013, **1**, 13742–13745.
162. A. K. Padhi, K. S. Nanjundaswamy and J. B. Goodenough, *J. Electrochem. Soc.*, 1997, **144**, 1188–1194.
163. Z. Gong and Y. Yang, *Energy Environ. Sci.*, 2011, **4**, 3223–3242.
164. K. Zhang, Z. Hu, H. Gao, H. Feng, F. Cheng, Z. Tao and J. Chen, *Sci. Adv. Mater.*, 2013, **5**, 1676–1685.
165. H. Yoo, M. Jo, B.-S. Jin, H.-S. Kim and J. Cho, *Adv. Energy Mater.*, 2011, **1**, 347–351.
166. S.-M. Oh, S.-W. Oh, C.-S. Yoon, B. Scrosati, K. Amine and Y.-K. Sun, *Adv. Funct. Mater.*, 2010, **20**, 3260–3265.
167. M. Pivko, M. Bele, E. Tchernychova, N. Z. Logar, R. Dominko and M. Gabersecek, *Chem. Mater.*, 2012, **24**, 1041–1047.
168. X. Rui, X. Zhao, Z. Lu, H. Tan, D. Sim, H. H. Hng, R. Yazami, T. M. Lim and Q. Yan, *ACS Nano*, 2013, **7**, 5637–5646.
169. S.-M. Oh, S.-T. Myung, J. B. Park, B. Scrosati, K. Amine and Y.-K. Sun, *Angew. Chem. Int. Ed.*, 2012, **51**, 1853–1856.
170. F. Wang, J. Yang, P. Gao, Y. NuLi and J. Wang, *J. Power Sources*, 2011, **196**, 10258–10262.
171. S. K. Martha, J. Grinblat, O. Haik, E. Zinigrad, T. Drezen, J. H. Miners, I. Exnar, A. Kay, B. Markovskiy and D. Aurbach, *Angew. Chem. Int. Ed.*, 2009, **48**, 8559–8563.
172. H. Wang, Y. Yang, Y. Liang, L.-F. Cui, H. Sanchez-Casalogue, Y. Li, G. Hong, Y. Cui and H. Dai, *Angew. Chem. Int. Ed.*, 2011, **50**, 7364–7368.
173. R. von Hagen, H. Lorrman, K.-C. Möller and S. Mathur, *Adv. Energy Mater.*, 2012, **2**, 553–559.
174. Y.-K. Sun, S.-M. Oh, H.-K. Park and B. Scrosati, *Adv. Mater.*, 2011, **23**, 5050–5054.
175. C. A. J. Fisher, N. Kuganathan and M. S. Islam, *J. Mater. Chem. A*, 2013, **1**, 4207–4214.
176. Y. Li, Z. Gong and Y. Yang, *J. Power Sources*, 2007, **174**, 528–532.
177. M. Kuzma, S. Devaraj and P. Balaya, *J. Mater. Chem.*, 2012, **22**, 21279–21284.
178. G. He and A. Manthiram, *Adv. Funct. Mater.*, 2014, DOI: 10.1002/adfm.201400610.
179. T. Muraliganth, K. R. Stroukoff and A. Manthiram, *Chem. Mater.*, 2010, **22**, 5754–5761.
180. S. Zhang, Z. Lin, L. Ji, Y. Li, G. Xu, L. Xue, S. Li, Y. Lu, O. Toprakci and X. Zhang, *J. Mater. Chem.*, 2012, **22**, 14661–14666.
181. P. G. Bruce, S. A. Freunberger, L. J. Hardwick and J.-M. Tarascon, *Nat. Mater.*, 2012, **11**, 19–29.
182. M. Leskes, N. E. Drewett, L. J. Hardwick, P. G. Bruce, G. R. Goward and C. P. Grey, *Angew. Chem. Int. Ed.*, 2012, **124**, 8688–8691.
183. R. Black, B. Adams and L. F. Nazar, *Adv. Energy Mater.*, 2012, **2**, 801–815.
184. Z. Wang, D. Xu, J. Xu and X. Zhang, *Chem. Soc. Rev.*, 2014, DOI: 10.1039/C3CS60248F.
185. F. Cheng and J. Chen, *Acta Chim. Sin.*, 2013, **71**, 473–477.
186. M. K. Debe, *Nature*, 2012, **486**, 43–51.
187. T. Yu, D. Y. Kim, H. Zhang and Y. Xia, *Angew. Chem. Int. Ed.*, 2011, **50**, 2773–2777.
188. S. Guo, S. Zhang and S. Sun, *Angew. Chem. Int. Ed.*, 2013, **52**, 8526–8544.
189. Y. Liang, H. Wang, J. Zhou, Y. Li, J. Wang, T. Regier and H. Dai, *J. Am. Chem. Soc.*, 2012, **134**, 3517–3523.
190. Z. Awaludin, M. Suzuki, J. Masud, T. Okajima and T. Ohsaka, *J. Phys. Chem. C*, 2011, **115**, 25557–25567.
191. S.-Y. Huang, P. Ganesan, S. Park and B. N. Popov, *J. Am. Chem. Soc.*, 2009, **131**, 13898–13899.
192. F. Cheng, T. Zhang, Y. Zhang, J. Du, X. Han and J. Chen, *Angew. Chem. Int. Ed.*, 2013, **52**, 2474–2477.
193. M. S. El-Deab and T. Ohsaka, *Angew. Chem. Int. Ed.*, 2006, **45**, 5963–5966.
194. I. Roche, E. Chaînet, M. Chatenet and J. Vondrák, *J. Phys. Chem. C*, 2006, **111**, 1434–1443.
195. A. Débart, A. J. Paterson, J. Bao and P. G. Bruce, *Angew. Chem. Int. Ed.*, 2008, **47**, 4521–4524.
196. P. Źóltowski, D. M. Dražić and L. Vorkapić, *J. Appl. Electrochem.*, 1973, **3**, 271–283.
197. M. M. Najafpour, T. Ehrenberg, M. Wiechen and P. Kurz, *Angew. Chem. Int. Ed.*, 2010, **49**, 2233–2237.
198. Y. Umena, K. Kawakami, J.-R. Shen and N. Kamiya, *Nature*, 2011, **473**, 55–60.
199. M. Wiechen, I. Zaharieva, H. Dau and P. Kurz, *Chem. Sci.*, 2012, **3**, 2330–2339.
200. D. A. Tompsett, S. C. Parker and M. S. Islam, *J. Am. Chem. Soc.*, 2014, **136**, 1418–1426.
201. F. Cheng, J. Shen, W. Ji, Z. Tao and J. Chen, *ACS Appl. Mater. Interfaces*, 2009, **1**, 460–466.
202. L. Mao, D. Zhang, T. Sotomura, K. Nakatsu, N. Koshiba and T. Ohsaka, *Electrochim. Acta*, 2003, **48**, 1015–1021.
203. B. Klápště, J. Vondrák and J. Velická, *Electrochim. Acta*, 2002, **47**, 2365–2369.
204. W. Sun, A. Hsu and R. Chen, *J. Power Sources*, 2011, **196**, 4491–4498.

205. C. Li, W. Ji, J. Chen and Z. Tao, *Chem. Mater.*, 2007, **19**, 5812–5814.
206. W. Li, C. Li, C. Zhou, H. Ma and J. Chen, *Angew. Chem. Int. Ed.*, 2006, **45**, 6009–6012.
207. Q. Wu, L. Jiang, L. Qi, E. Wang and G. Sun, *Int. J. Hydrogen Energy*, 2014, **39**, 3423–3432.
208. L. Zhang, X. Zhang, Z. Wang, J. Xu, D. Xu and L. Wang, *Chem. Commun.*, 2012, **48**, 7598–7600.
209. Q. Li, P. Xu, B. Zhang, H. Tsai, J. Wang, H.-L. Wang and G. Wu, *Chem. Commun.*, 2013, **49**, 10838–10840.
210. Y. Cao, Z. Wei, J. He, J. Zang, Q. Zhang, M. Zheng and Q. Dong, *Energy Environ. Sci.*, 2012, **5**, 9765–9768.
211. T. T. Truong, Y. Liu, Y. Ren, L. Trahey and Y. Sun, *ACS Nano*, 2012, **6**, 8067–8077.
212. D. Oh, J. Qi, Y.-C. Lu, Y. Zhang, Y. Shao-Horn and A. M. Belcher, *Nat. Commun.*, 2013, **4**, 2756.
213. E. M. Benbow, S. P. Kelly, L. Zhao, J. W. Reutenauer and S. L. Suib, *J. Phys. Chem. C*, 2011, **115**, 22009–22017.
214. M. De Koninck, S.-C. Poirier and B. Marsan, *J. Electrochem. Soc.*, 2006, **153**, A2103–A2110.
215. J. S. Armijo, *Oxid. Met.*, 1969, **1**, 171–198.
216. H. Wang, F. Cheng, Z. Tao, J. Liang and J. Chen, *Chem. J. Chinese Univ.*, 2011, **32**, 595–600.
217. J. Du, Y. Pan, T. Zhang, X. Han, F. Cheng and J. Chen, *J. Mater. Chem.*, 2012, **22**, 15812–15818.
218. S. Ma, L. Sun, L. Cong, X. Gao, C. Yao, X. Guo, L. Tai, P. Mei, Y. Zeng, H. Xie and R. Wang, *J. Phys. Chem. C*, 2013, **117**, 25890–25897.
219. H. Wang, Y. Yang, Y. Liang, G. Zheng, Y. Li, Y. Cui and H. Dai, *Energy Environ. Sci.*, 2012, **5**, 7931–7935.
220. Y. Zhao, L. Xu, L. Mai, C. Han, Q. An, X. Xu, X. Liu and Q. Zhang, *Proc. Natl. Acad. Sci. USA*, 2012, **109**, 19569–19574.
221. A. Débart, J. Bao, G. Armstrong and P. G. Bruce, *J. Power Sources*, 2007, **174**, 1177–1182.
222. J. Xu, D. Xu, Z. Wang, H. Wang, L. Zhang and X. Zhang, *Angew. Chem. Int. Ed.*, 2013, **52**, 3887–3890.
223. H. Feng, J. Du, X. Han, F. Cheng and J. Chen, *Chinese J. Inorg. Chem.*, 2013, **29**, 1617–1625.
224. X. Han, Y. Hu, J. Yang, F. Cheng and J. Chen, *Chem. Commun.*, 2014, **50**, 1497–1499.
225. M. M. Lee, J. Teuscher, T. Miyasaka, T. N. Murakami and H. J. Snaith, *Science*, 2012, **338**, 643–647.
226. J. Burschka, N. Pellet, S.-J. Moon, R. Humphry-Baker, P. Gao, M. K. Nazeeruddin and M. Grätzel, *Nature*, 2013, **499**, 316–319.
227. M. Liu, M. B. Johnston and H. J. Snaith, *Nature*, 2013, **501**, 395–398.
228. Y. Liang, Y. Li, H. Wang, J. Zhou, J. Wang, T. Regier and H. Dai, *Nat. Mater.*, 2011, **10**, 780–786.
229. J.-S. Lee, G. S. Park, H. I. Lee, S. T. Kim, R. Cao, M. Liu and J. Cho, *Nano Lett.*, 2011, **11**, 5362–5366.
230. J. Li, N. Wang, Y. Zhao, Y. Ding and L. Guan, *Electrochem. Commun.*, 2011, **13**, 698–700.
231. Y. Qin, J. Lu, P. Du, Z. Chen, Y. Ren, T. Wu, J. T. Miller, J. Wen, D. J. Miller, Z. Zhang and K. Amine, *Energy Environ. Sci.*, 2013, **6**, 519–531.
232. K.-N. Jung, J.-I. Lee, S. Yoon, S.-H. Yeon, W. Chang, K.-H. Shin and J.-W. Lee, *J. Mater. Chem.*, 2012, **22**, 21845–21848.
233. S. Liu, Y. Zhu, J. Xie, Y. Huo, H. Y. Yang, T. Zhu, G. Cao, X. Zhao and S. Zhang, *Adv. Energy Mater.*, 2014, DOI: 10.1002/aenm.201301960.
234. H. Y. Lee and J. B. Goodenough, *J. Solid State Chem.*, 1999, **144**, 220–223.
235. J.-K. Chang, Y.-L. Chen and W.-T. Tsai, *J. Power Sources*, 2004, **135**, 344–353.
236. C.-C. Hu and T.-W. Tsou, *Electrochem. Commun.*, 2002, **4**, 105–109.
237. V. Subramanian, H. Zhu and B. Wei, *J. Power Sources*, 2006, **159**, 361–364.
238. E. Macheffaux, T. Brousse, D. Bélanger and D. Guyomard, *J. Power Sources*, 2007, **165**, 651–655.
239. S. W. Donne, A. F. Hollenkamp and B. C. Jones, *J. Power Sources*, 2010, **195**, 367–373.
240. S. Devaraj and N. Munichandraiah, *J. Electrochem. Soc.*, 2007, **154**, A901–A909.
241. H. Xia, J. Feng, H. Wang, M. O. Lai and L. Lu, *J. Power Sources*, 2010, **195**, 4410–4413.
242. J. Yuan, Z. Liu, S. Qiao, X. Ma and N. Xu, *J. Power Sources*, 2009, **189**, 1278–1283.
243. E. Beaudrouet, A. Le Gal La Salle and D. Guyomard, *Electrochim. Acta*, 2009, **54**, 1240–1248.
244. J. Yan, Z. Fan, T. Wei, W. Qian, M. Zhang and F. Wei, *Carbon*, 2010, **48**, 3825–3833.
245. X. Dong, W. Shen, J. Gu, L. Xiong, Y. Zhu, H. Li and J. Shi, *J. Phys. Chem. B*, 2006, **110**, 6015–6019.
246. H. Jiang, L. Yang, C. Li, C. Yan, P. S. Lee and J. Ma, *Energy Environ. Sci.*, 2011, **4**, 1813–1819.
247. Jaidev, R. I. Jafri, A. K. Mishra and S. Ramaprabhu, *J. Mater. Chem.*, 2011, **21**, 17601–17605.
248. D. Zhu, Y. Wang, G. Yuan and H. Xia, *Chem. Commun.*, 2014, **50**, 2876–2878.
249. R. Amade, E. Jover, B. Caglar, T. Mutlu and E. Bertran, *J. Power Sources*, 2011, **196**, 5779–5783.